Received: 24 May 2022 | Revised: 10 October 2022 | Accepted: 12 October 2022

DOI: 10.1111/jmg.12700

ORIGINAL ARTICLE

Journal of METAMORPHIC GEOLOGY WILEY

# Petrochronology of polygenetic white micas (Naxos, Greece)

**Igor M. Villa**[1,2] | **Johannes Glodny**[3] | **Alexandre Peillod**[4] | **Alasdair Skelton**[5] | **Uwe Ring**[5]

[1]Institut für Geologie, Universität Bern, Bern, Switzerland

[2]Centro Universitario Datazioni e Archeometria, Università di Milano Bicocca, Milan, Italy

[3]GFZ German Research Centre for Geosciences, Potsdam, Germany

[4]Institute of Applied Geosciences (AGW), Karlsruhe Institute of Technology (KIT), Karlsruhe, Germany

[5]Department of Geological Sciences, Stockholm University, Stockholm, Sweden

**Correspondence**
Igor M. Villa, Centro Universitario Datazioni e Archeometria, Università di Milano Bicocca, 20126 Milan, Italy.
Email: igor@geo.unibe.ch

Handling Editor: Prof. Clare Warren

## Abstract

Naxos in the Greek Cyclades preserves a type example of polymetamorphism. The southern and northern parts of the island record different Tertiary *P*–*T* histories between Eocene and Miocene times, including a blueschist facies event, one or more amphibolite/greenschist facies overprint(s) and contact metamorphism. Age attributions for these events are inconsistent in the literature. Here, we propose a new approach that combines electron probe microanalyzer (EPMA) characterization of the white mica (WM) with $^{39}$Ar-$^{40}$Ar–Rb-Sr multichronometry. Textural–petrographic–compositional observations reveal that the polygenetic WM consists of five different generations: pre-Eocene relicts, paragonite, high-Si phengite, low-Si phengite and muscovite. EPMA mapping of four WM samples, previously analysed by Rb-Sr, reveals major element compositions heterogeneous down to the μm scale. Each WM consists of chemically distinct generations, documenting submicron-scale retrogression of high-pressure (HP) phengite grains to muscovite. Four WM samples from a N-S traverse across the island were analysed by $^{39}$Ar-$^{40}$Ar stepheating, comparing coarse and fine sieve size fractions to obtain overdetermined K-Ar systematics. Fine sieve fractions are richer in Cl than coarse ones. Linear arrays in Cl/K-age isotope correlation diagrams show two predominant WM generations (one Cl-poor at ca. 38 Ma and one Cl-rich at <20 Ma). A lower-grade sample from southern Naxos was less pervasively recrystallized, provides older ages and preserves at least three WM generations, including a relict WM with a pre-Palaeocene K-Ar age, consistent with the high Ar retentivity of WM in the absence of complete recrystallization. The age of the Cl-poor end-member WM approximates the age of the HP event, 38 Ma. Ar inheritance in Cretaceous mica relicts is heterogeneous at the single-grain scale. Comparing the degassing rates of the WM fractions rules out 'multidomain' diffusion. As no sample is monomineralic, the degassing rate of each polygenetic mica is instead controlled by the mass balanced sum of the unrelated rate constants of its constituent minerals. Given the commonness of zoned and composite micas, the approach detailed here is potentially useful for reconstructing polyphase metamorphic histories worldwide.

**KEYWORDS**
$^{39}$Ar-$^{40}$Ar–Rb-Sr multichronometry, Cycladic Blueschist Unit, geochronology, petrochronology, white mica

## 1 | INTRODUCTION

Dating the different events recorded in minerals that underwent a complex metamorphic evolution has long been fraught with difficulties, and only recently, multichronometry and petrochronology have brought decisive progress (see, e.g., the recent studies quoted by Bosse and Villa, 2019). The term 'petrochronology' was first used by Kylander-Clark et al. (2013), who discussed its application to zircon and monazite, both well-known to be immune from thermally induced Pb loss. Bosse and Villa (2019) pointed out that in many cases, the relative rates of thermally induced diffusion and of fluid-assisted recrystallization encourage the use of micas as petrochronometers. The key feature of petrochronology is creating the context between analytical techniques that have existed for a long time but as separate and non-communicating disciplines. Such techniques are microstructural analysis, high-resolution chemical mapping, multichronometry and the full potential provided by the $^{39}$Ar-$^{40}$Ar technique.

The case history of Naxos Island (Greece) is particularly appealing, as it is a prime example of polymetamorphism. Its rocks record two separate pressure–temperature (*P*–*T*) paths: one reaching high-pressure (HP) conditions followed by exhumation and retrogression; at a later time, the island was affected by contact metamorphism, caused by a granitoid intrusion (e.g. Peillod et al., 2017) and unrelated to the *P*–*T* path of the HP event. The age of the youngest event, the Miocene contact metamorphism, was estimated by Keay et al. (2001) as ca. 12 Ma by U-Pb dating of zircon grains from the granite intrusives responsible for it. The high-grade part of the *P*–*T* path has been dated by three studies, all of which provided different age estimates: Wijbrans and McDougall (1986, 1988) proposed the HP peak at ca. 50 Ma; Peillod et al. (2017) assigned it an age of 38–42 Ma; Cao et al. (2018) favoured an age of 44–47 Ma. We argue that this discrepancy is due to the combined effect of petrographic and isotopic inheritance, of subsequent GS retrogression and of the Miocene contact metamorphism.

The applicability of even earlier studies is less clearly established for those papers that were based on unreliable and discontinued dating methods (such as bulk K-Ar). What all of the cited studies did observe was that multiple white mica (WM) generations were preserved in most samples. In order to clarify the causes of the discrepancies and to propose a reliable age assignment, we applied the $^{39}$Ar-$^{40}$Ar technique to the same sample separates analysed by Rb-Sr by Peillod et al. (2017). By redundantly analysing different grainsizes of the same minerals already analysed by a different parent–daughter isotopic system, we aimed for an overdetermined data set, which would provide more robust answers to the following questions: Why do different studies derive inconsistent results from the same rocks? Can a consistent chronology be achieved by multichronometry? Do the K-Ar and Rb-Sr isotopic systems record the same event, and if so, which one? Can Rb-Sr contribute to distinguish between excess Ar and Ar inheritance? At what scale can the preservation of petrographic relicts be observed, and how can it bias interpretations? What role can be assigned to diffusive re-equilibration of major and trace elements, and what other isotope transport mechanisms effect a rejuvenation of HP and relict minerals?

Here we show that disentangling the ages of the different WM generations can be achieved by combining textural microanalysis, electron microprobe element mapping, multichronometric Rb-Sr versus K-Ar comparisons, differential Ar release plots and common denominator three-isotope correlation (CDTIC) diagrams. Studies that do not contain all of these essential pieces of information are likely to provide an underconstrained chronological interpretation.

## 2 | GEOLOGICAL SETTING

The island of Naxos in the Cyclades is part of the Hellenide orogen in the eastern Mediterranean. The Hellenides form an arcuate orogen to the north of the present-day active Hellenic margin (Figure 1, inset), which marks the site of NNE-ward subduction of the African plate beneath Eurasia. The Cycladic Blueschist Unit (CBU) is the major tectonic unit in the Cyclades and represents a world-class natural laboratory for studying HP rocks and their multiple subsequent lower-pressure metamorphic overprints. In the Cyclades, the Hellenide Orogeny commenced in the early Cenozoic causing subduction and sustained HP metamorphism between ca. 53 and 30 Ma (Tomaschek et al., 2003; Ring, Glodny, et al., 2007; Glodny & Ring, 2022, and references therein). Lower-pressure retrogression of the HP rocks has been

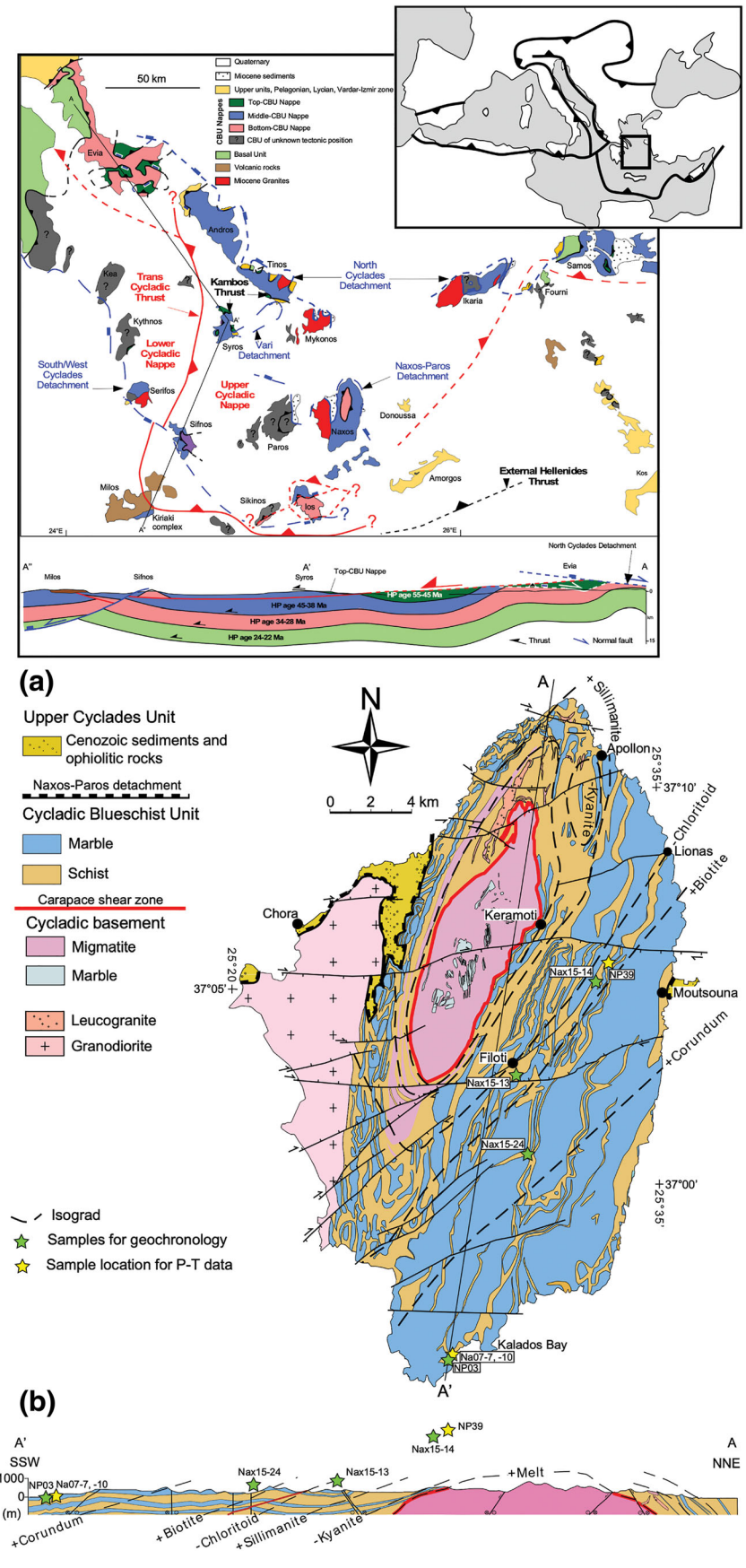


**FIGURE 1** (a) Tectonic map of the Cyclades showing the spatial arrangement of outcrops of three Cycladic Blueschist Unit (CBU) high-pressure (HP) nappes in the Cyclades. The cross-section illustrates schematically the four HP belts with their proposed ages for peak-HP metamorphism and their relation to the trans Cycladic Thrust. Inset on upper right shows main subduction zones in the Mediterranean and position of the Cyclades map shown in (a) north of the Hellenic subduction zone. (b, c) Geologic/tectonic map and N-S cross-section of Naxos (modified after Peillod et al., 2017). Metamorphic zones range from the migmatitic core (approximately 700°C) to greenschist grade in the south of the island. Yellow stars: samples used by Peillod et al. (2017), Peillod, Majka, et al. (2021),and Peillod, Tehler, et al. (2021) for *P–T* path analyses. Green stars: aliquots of the Peillod et al. (2017) samples analysed in the present work

dated at seemingly separate times in the literature. In Samos and western Anatolia, a greenschist facies assemblage associated with the emplacement of the CBU onto the greenschist facies Menderes nappes has been proposed to be between 43 and 34 Ma old (Çetinkaplan et al., 2020; Hetzel & Reischmann, 1996; Ring & Layer, 2003; Ring, Will, et al., 2007). Another retrogressive greenschist facies assemblage in the passive margin sequence in South Syros and South Naxos was proposed to be of Oligocene age (ca. 36–27 Ma: Maluski et al., 1987; Peillod et al., 2017; Skelton et al., 2019). Finally, a regionally widespread Miocene greenschist/amphibolite facies metamorphic overprint was assigned ca. 22–11 Ma age (Glodny & Ring, 2022; Jolivet & Brun, 2010; Kumerics et al., 2005; Wijbrans & McDougall, 1986, 1988). The latter is probably associated with large-scale continental extension starting at ca. 23–21 Ma (Ring et al., 2010), accompanied by the intrusion of S- and I-type plutons between 17 and 11 Ma (Bolhar et al., 2010).

Glodny and Ring (2022) analysed the age pattern for HP and greenschist facies metamorphism and subdivided the CBU into three nappes (Figure 1, inset): (1) the Top-CBU Nappe with peak HP at 55–45 Ma, decompression from 44 to 39 Ma and a greenschist facies overprint starting at about 43 Ma; (2) the Middle-CBU Nappe with peak HP at about 47–38 Ma (with some ages as young as 34–33 Ma), followed by decompression at 39–30 Ma and a first greenschist facies overprint commencing by 33 Ma; and (3) the Bottom-CBU Nappe with peak HP metamorphism at 34–28 Ma, decompression at 27–24 Ma and a greenschist facies overprint by 25–18 Ma. This late greenschist facies overprint is detectable in all three CBU nappes and considered to be related to large-scale continental extension.

In this tectonochronologic scheme, the CBU rocks of Naxos would be made up by the Middle-CBU Nappe overlying the Cycladic basement as part of the Bottom-CBU Nappe (Figure 1). The CBU nappes are intruded by the I-type Naxos granodiorite. All these crystalline rocks are tectonically overlain by a non-metamorphic Upper unit (e.g. Kuhlemann et al., 2004) above the 23 to 8 Ma old extensional Naxos–Paros detachment (Brichau et al., 2006; Glodny & Ring, 2022; Seward et al., 2009).

The Middle-CBU Nappe is made by schist and marble, with some metabasalt lenses, representing a Permo-Mesozoic passive margin sequence. The Bottom-CBU Nappe is a migmatitic basement with high-grade marble (Figure 1). The passive margin sequence is tectonically separated from the basement and has southward dips to the south of the migmatite core (Linnros et al., 2019). Because of this tilt, the southeastern parts of the passive margin sequence escaped the strong Miocene metamorphism that caused the migmatization of the basement (see also below).

In general, the geochronology of the CBU is quite complex. Very recent studies (e.g. Gorce et al., 2021; Tual et al., 2022) support and reinforce the notion that one blueschist unit on one island, Syros, is 52 Ma old (Tomaschek et al., 2003); they also discover that in Syros itself different blueschist units differ by up to 10 Ma in age, as they do in Sifnos. The multimethod geochronological data (U-Pb, Sm-Nd, Lu-Hf, Rb-Sr, Ar-Ar) on Cycladic islands, particularly on Syros, gave ages consistent at the outcrop scale but regionally contrasting. Uunk et al. (2022, their Figure 9) further calculate four different PT paths for various units of these two close-by islands and, what is relevant for the present discussion, establish that each of these four units underwent HP conditions at a different time. In fact, there is no reason to assume that high-P metamorphism across the entire Cyclades was simultaneous since it was diachronous even on a single, 20 km-sized island. If and when all other Cycladic islands will be analysed with the same petrochronological approach will it be possible to compare ages that pertain to the same sequence of petrological events.

The metamorphic history of Naxos includes HP metamorphism (560–630°C and 15–20 kbar) in the Eocene (Cao et al., 2018; Peillod et al., 2017; Peillod, Majka, et al., 2021; Peillod, Tehler, et al., 2021; Wijbrans & McDougall, 1986, 1988). The HP rocks occur in SE Naxos, but ages related to the HP overprint occur throughout the passive margin sequence. Martin et al. (2006) obtained U-Pb zircon ages by secondary ion mass spectrometry, using a spatial resolution of 25 μm and proposed three distinct periods of zircon rim formation at ca. 70, 40 and 20 Ma (cf. Bolhar et al., 2017). In the south, the HP rocks were exhumed to mid-crustal levels and overprinted by greenschist facies metamorphism (360–420°C and 3.5–5.5 kbar) at 36–30 Ma (Avigad, 1998; Peillod et al., 2017). Zircon fission-track ages indicate that the HP rocks of SE Naxos were in the upper crust by the late Oligocene (Seward et al., 2009).

In central and northern Naxos, the passive margin sequence was overprinted by amphibolite facies metamorphism (Jansen & Schuiling, 1976; Lamont et al., 2020), and the basement underwent migmatization from about 18 to 12 Ma (Jansen & Schuiling, 1976; Ring et al., 2018; Vanderhaeghe, 2004; Vanderhaeghe et al., 2018). Jansen and Schuiling (1976) mapped six concentric metamorphic isograds indicating the strong thermal overprint with increasing temperatures towards the migmatite dome (Figure 1). Ring et al. (2018) argued for an age of about 14 Ma for isograd formation, and Linnros et al. (2019) showed that the formation of the isograds proceeded from south to north during ongoing extensional deformation. At a late stage S-type leuco- and

biotite granites intruded between 15 and 11 Ma, and the I-type granodiorite in western Naxos at 13 to 12 Ma (Bolhar et al., 2010).

The four WM samples that we studied are grain aliquots of the same hand-picked mica fractions studied by Peillod et al. (2017) from SE Naxos. Nax15-13 and Nax15-14 are a mylonitic calc-schist and a micaschist, respectively, both from the biotite-in zone. Nax15-24 is a marble near the corundum-in boundary, and Na07–10 is a blueschist facies calc-schist from Kalados bay at the southern tip of the island (Figure 1).

## 3 | ANALYTICAL METHODS

Samples were collected, and minerals separated, as described by Peillod et al. (2017). Polished sections of the rocks were studied by electron probe microanalyzer (EPMA) with a JEOL JXA-8530 field emission electron microprobe at GFZ Potsdam and at the Department of Earth Sciences, Uppsala University, following Müller et al. (2017) and Skelton et al. (2019), respectively. The JEOL PC-EMPA application software (version 1.5.0.4) was used. Running conditions were 15 kV and 20 nA, with a beam size of 0.5–10 μm. Both backscattered electron (BSE) maps and individual element maps were obtained.

Since the scale of the intergrown WM retrogressive replacements was <<10 μm in all cases (see Section 4.1), it was realized that $^{39}$Ar-$^{40}$Ar dating by laser microprobe had no chance of spatially resolving the individual mica generations, as 'single-grain analyses' of such finely intergrown materials are actually analyses of a composite population of different minerals. WM samples, for which sufficient material of at least two of the size fractions already analysed by Peillod et al. (2017) remained, were irradiated in the McMaster University research reactor (Canada), carefully avoiding Cd shielding (which would destroy the information about the Cl/K ratio), using Fish Canyon sanidine as irradiation monitor with an assumed age of 28.172 Ma (Rivera et al., 2011). Stepwise heating followed the procedures described in Villa et al. (2000); the fine fraction of each sample was heated with the same schedule as the coarse one. Moreover, the three NAX15 samples were heated with the same schedule, whereas Na07-10 followed a slightly different one. The minimum sample size to achieve a useful precision of 10% on the Cl/K ratio was estimated as 5 mg on the basis of past experience with the low Cl concentrations of WMs (Villa et al., 2014), supporting the suspicion that the usual laser pit size of ca. 30 μm is both too large (not being able to spatially resolve intergrowths) and too small (not being able to degas sufficient amounts of $^{38}Ar_{Cl}$ for a useful mica fingerprinting). By contrast, furnace heating of mg-sized aliquots is capable of producing enough $^{38}Ar_{Cl}$ while at the same time exploiting the differential Ar release of phengite and muscovite (Wijbrans & McDougall, 1986; see also Figure 2 and Section 4.3. below), which results in an effective size resolution below 1 μm (Müller et al., 2002). As paragonite has a yet different differential Ar release (Allaz et al., 2011), we expect additional options to resolve that mica variety as well. Analysing two sieve fractions of the same rock results in an overdetermined system, which allows the assessment of the relative importance of recrystallization and diffusion. The coarse sieve sizes were 250–355 μm, the fine ones 160–250 μm (for NAX15-13 and -14), respectively, and 90–160 μm (for Na07-10 and NAX15-24). The results are presented in the supporting information Table S1.

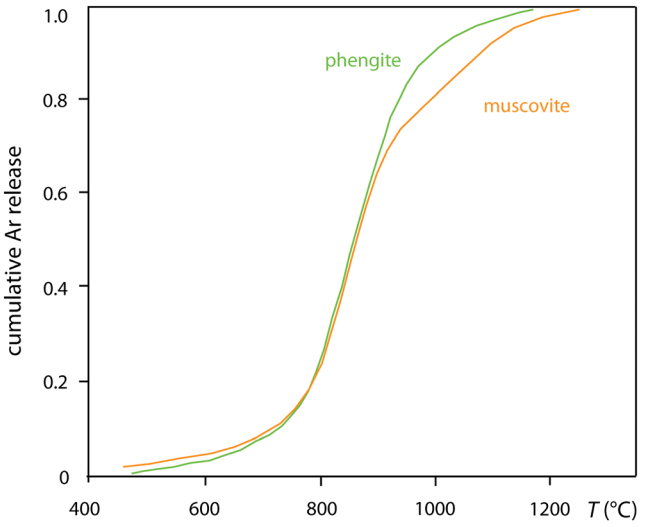


FIGURE 2 First observation of the difference in gas release from mixed mica generations in Naxos (redrawn after Wijbrans & McDougall, 1986)

## 4 | RESULTS AND DISCUSSION

The choice of relevant results to be presented is a function of the interpretation of the data. The petrochronological approach requires not just mass spectrometric results but, above all, establishing the context between chemical–textural microanalysis and the petrological framework. As already documented by Wijbrans and McDougall (1986), Ar inheritance is ubiquitous in the Naxos samples, as the Ar record is not reset in HP phengite by the Miocene high temperature (HT) overprint except in one migmatite from the metamorphic core (Wijbrans & McDougall, 1986, their sample 81-556). The

resulting isotopic complexity requires a thorough exploitation of all the interpretive insight provided by $^{39}Ar$-$^{40}Ar$ systematics in order to explain the similarities and differences of the Rb-Sr chronometers with the K-Ar chronometers and to derive a robust disentanglement of the chronological data.

## 4.1 | Chemical microanalysis

Textural observations reveal that sieve fractions consist of a polygenetic population of five different WM generations: pre-Eocene relicts, paragonite, high-Si phengite, low-Si phengite and muscovite. EPMA analyses confirm the coexistence of multiple mica generations (Cao et al., 2018; Peillod et al., 2017) in every analysed sample (Figure 3). The maps mainly show relative compositional variations; for the present investigation, this is sufficient to draw home the point that heterochemical generations are intergrown at a scale <<10 μm. The sample farthest from the HT core, Na07-10, contains a relict muscovite and two HP micas, phengite and paragonite (Peillod et al., 2017). Paragonite also is observed south of the corundum-in isograd (NP03, Na30A, N32C, N9A; Peillod et al., 2017; Cao et al., 2018) and further north of the corundum-in isograd (NAX15-24; Peillod et al., 2017). These authors provided the petrological identification and the quantitative EPMA compositional analyses. Closer to the HT core, north of the biotite-in isograd, samples NAX15-13 and -14 no longer contain a relict generation; subordinate HT muscovite is formed at the expense of the HP phengite. It is essential to stress that the layer-by-layer retrograde substitution reaction, forming muscovite at the expense of phengite, is observed to occur at the sub-μm scale. This makes laser microprobe dating (e.g. Wijbrans et al., 1990) extremely likely to obtain mixed ages, as the

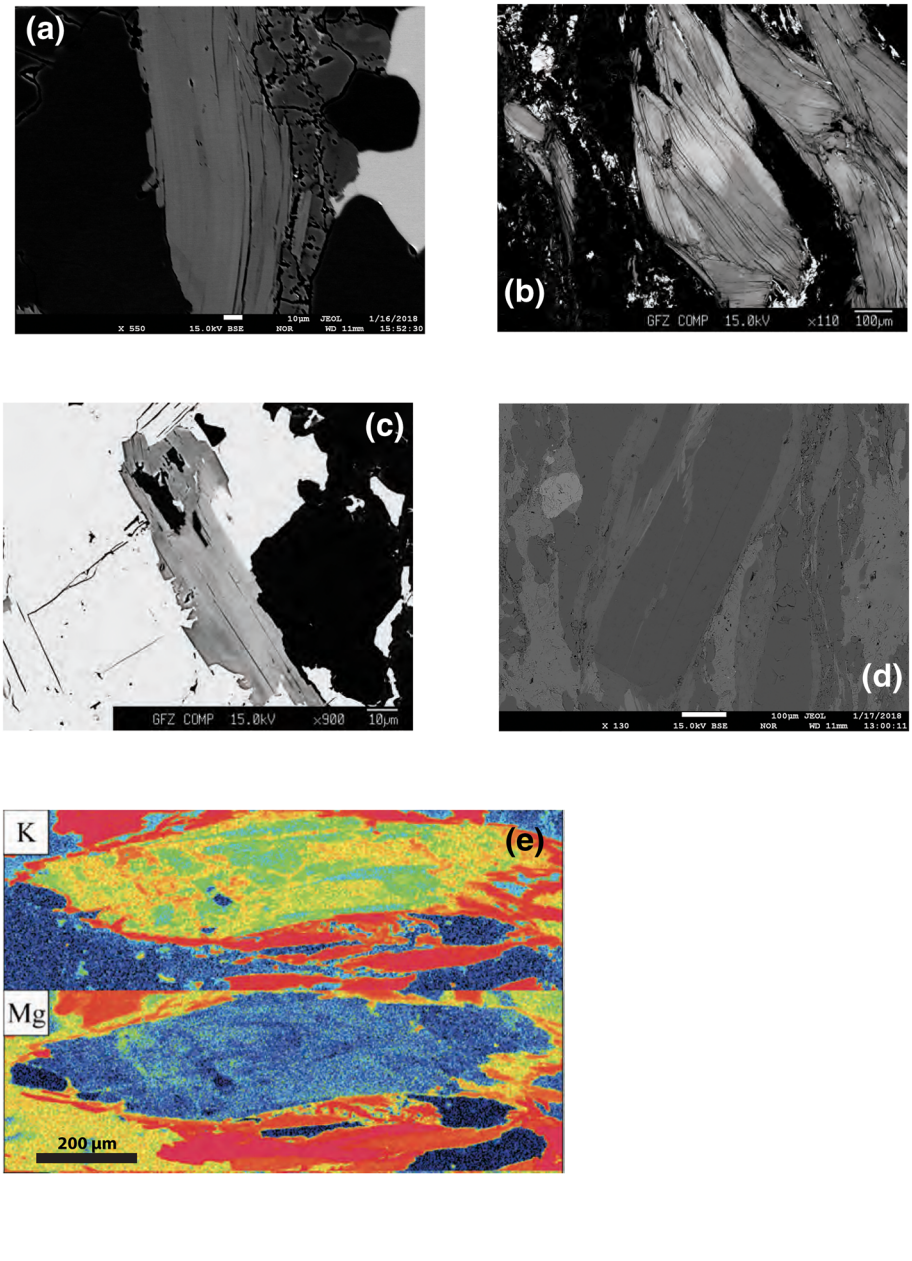


**FIGURE 3** Backscattered electron maps for (a) sample NAX15-13 (scale bar 10 μm); note: phengite–muscovite layer-by-layer intergrowths visible at the μm scale as bright and dark grey layers, respectively; (b) NAX 15-14 (scale bar 100 μm); (c) patchy muscovite–paragonite intergrowth from NAX15-24 (scale bar 10 μm); (d) Na07–10 (scale bar 100 μm); (e) K and Mg element maps of a mm-sized single white mica grain from NAX15-24 (field of view 1 mm). Variations in the Mg substitution demonstrate the scale of heterochemical intergrowths. Patchy substoichiometric K concentrations identify partly altered, intergrown clay-like layers.

diameter of the laser beam is up to 2 orders of magnitude larger than the scale of the targeted microstructures. The present capabilities of analytical instrumentation thus fall far short of the 'Goldilocks zone' of Villa (2022). Whenever this occurs, excessively large laser pits produce mixed ages devoid of geological significance.

## 4.2 | Chemical correlation diagrams

Neutron irradiation produces rare gas isotopes from several elements (Merrihue, 1965; Reynolds, 1963). Ever since the early days of rare gas geochronology, systematic information about carrier phases in polymineralic systems was derived from CDTIC diagrams. In such a diagram, the coordinate axes are two isotope ratios that have a common denominator (Reynolds, 1963). The convenience of having a common denominator is that binary mixtures always yield linear arrays (e.g., Villa, 2001). The diagnostic tool provided by CDTIC diagrams can thus be applied to disentangle both natural phase mixtures (due to metamorphic reactions or even just to imperfect separation) and artificial mixtures (Villa et al., 1996; Villa & Hanchar, 2017). In $^{39}Ar$-$^{40}Ar$ dating, the choice of $^{39}Ar$ as a common denominator is most convenient; however, other choices for the denominator isotope are algebraically equivalent (Turner, 1988).

The production of Ar isotopes from target elements K, Cl and Ca (the latter two sometimes improperly called 'interfering reactions') allows a twofold use: firstly, assessing whether the K concentration matches stoichiometry and secondly, determining Cl and Ca concentrations. The $^{38}Ar_{Cl}/^{39}Ar_K$ and $^{37}Ar_{Ca}/^{39}Ar_K$ ratios faithfully mirror Cl/K and Ca/K, respectively, whereby these two element ratios fingerprint the compositional signature of the analysed materials. It has been demonstrated that in artificial binary mineral mixtures (Villa et al., 1996), the combination of the Cl/K and Ca/K in a CDTIC diagram diagnoses the existence of a mixture and can identify the end-members when the Ca/K or Cl/K element ratios are independently known.

Common denominator diagrams are a prime tool to diagnose petrologic equilibrium, as any incomplete petrological reaction produces a mixture of at least two heterochemical phases (the relict primary mineral and one or more secondary product phases). In a simple two-component mixture, the interpretation of a CDTIC is straightforward (e.g. Villa & Hanchar, 2017, their Figure 7; Allaz et al., 2011, their Figure 9). A third mixing component results in deviations of the data points from a linear correlation; a more detailed discussion is provided by Villa (2001).

In the case of the inventory of WMs in Naxos, Siebenaller et al. (2013) observed that fluid inclusions with the highest homogenization temperatures (i.e. those trapped at the highest metamorphic conditions) also have the highest salinities, that is, Cl concentrations. They further argued that the hottest fluids were exsolved during the HT event related to magma crystallization at or after 17 Ma. The link between distinguishable Cl concentrations in the circulating metamorphic fluids and phengite–muscovite retrogression was independently observed in the Western Alps (Herviou et al., 2021; Villa et al., 2014), establishing the Cl/K ratio as a very valuable diagnostic tool to unravel petrological mixtures. If, in addition to phengite and muscovite, paragonite is also present, its contribution can be proxied by $^{37}Ar$ (Allaz et al., 2011).

Figure 4 illustrates the behaviour found in all Naxos samples. The complexity of any diagram (including CDTIC) depends on the number of coexisting mineral phases. Many WM samples (e.g. Heri et al., 2014) consist of more than two generations, and accordingly, their correlation diagrams appear chaotic at first sight. Among the Naxos micas, high-grade sample NAX15-14 most closely approaches a two-component mixture, with relatively minor contribution from additional phases and is therefore discussed in more detail. The Ca/Cl/K correlation diagram for NAX15-14 (Figure 4b) most clearly reveals two peculiarities: (A) both size fractions form a rather well-defined alignment with a positive slope, which is certain proof that the degassed material is not a homogeneous, monomineralic phase and (B) the chemical signature of the two grain sizes differs by a factor of 2 (also evident from the bulk sum of [Cl] and [Ca] in Table S1), meaning that the crushing and sieving in the laboratory resulted in a detectable variation of the phase inventory of the sieve fractions. Both observations were expected: A fingerprint of the well-understood phengite–muscovite mixture in Naxos samples (Wijbrans & McDougall, 1986) was actually sought for, and (A) provides it; the fact that crushing a heterogeneous mica population produces heterochemical sieve fractions is not surprising, as (B) had been documented in detail by Heri et al. (2014). The mechanical mechanism for this observed disproportionation is unknown.

The lower-grade samples NAX15-24 and Na07-10 also contain small amounts of paragonite. Since its modal abundance is low in the present samples, recognizing the Ar bearing the paragonite signature is difficult, and even more so disentangling its contribution from that of phengite and muscovite. Future studies may discover samples with a more user-friendly phase assemblage and successfully constrain the age of paragonite growth.

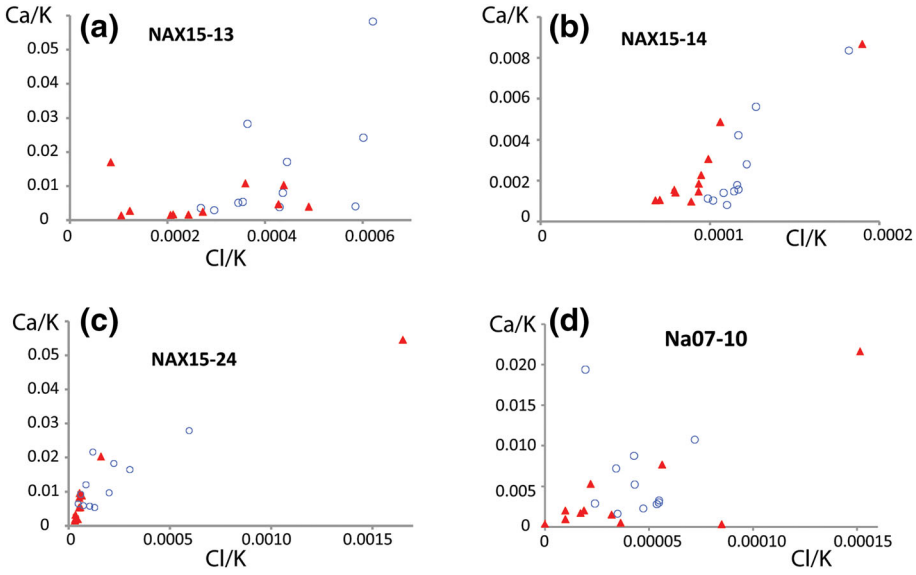


**FIGURE 4** Ca/K–Cl/K ($^{37}Ar_{Ca}/^{39}Ar_K$ vs. $^{38}Ar_{Cl}/^{39}Ar_K$) common denominator three-isotope correlation diagrams for white mica samples. For all four samples, both the coarse sieve fraction (filled triangles) and the fine one (open circles) consist of at least two heterochemical phases, one with low and one with high Ca/K and Cl/K ratios, with different mass fractions in the two sieve fractions. As the axes have a common denominator, mixing these two end-members results in a linear array (Villa, 2001). The deviations from an ideal linearity indicate that while two phases are predominant, minor phases also contribute a small but detectable amount of gas.

## 4.3 | In vacuo degassing rates

An additional diagnostic tool is a quantification of the degassing rates in the two size fractions. As the degassing rate, $k_A$, is a function of temperature, $T$, its dependence on $T$ can be displayed in an Arrhenius diagram (Figure 5). Arrhenius diagrams can be used to examine the temperature dependence of the rate of any process, in which the kinetic energy of the particles participating in the process, $kT$, is compared with the threshold energy that activates the process, $Q$. A particular case of Arrhenius diagram is a plot of the diffusivity, $D$, or of the frequency factor, $D/a^2$; however, it must be made clear that the assumption of equivalence between the Arrhenian rate constant $k_A$ and the true Fickian diffusivity needs not to hold true in the general case. The interpretation of $k_A$ as Fickian diffusivity requires additional constraints. It was recently proposed (Kula & Spell, 2012; see the discussion by Villa, 2021) that $k_A$ is always identical with $D/a^2$, and that its Arrhenian non-linearity is supposedly proof that discrete diffusion 'domains', up to ≥3 orders of magnitude smaller than the crystallographically coherent grain size, control the Ar release of mica in vacuo and cause the kinked Arrhenius trajectories. A similar claim for K-feldspar has been conclusively disproved (Chafe et al., 2014); the correction of this misconception has now been extended to the mica case (Villa, 2021).

The overdetermined quartet of the present mica samples shows a reproducible pattern, which provides unambiguous constraints on the in vacuo degassing mechanism of hydrous minerals such as WM (Figure 5). The 'Discrete Domain Theory' predicts the Arrhenian trajectories that two sieve size fractions of the same sample must have. This is shown in Figure 5a, which shows the Arrhenian trajectory predicted for two sieve sizes of one Naxos sample chosen arbitrarily (since all four samples discussed here follow the same pattern, this choice is unimportant). Crosses (coarse sieve fraction) and circles (fine sieve fractions) model the convoluted release of several 'diffusion domains', ranging in size from some very small grain radius $r_0$ to, at most, $r_{max}$, the grain radius of the sieve fraction. Whether $r_0$ is smaller or larger than the cutoff value for physical legitimacy due to $^{39}Ar$ recoil is unimportant for the present argument. All aliquots of the same sample are expected to share the same 'domain' structure; in particular, all larger sieve fractions necessarily degas exactly like the smaller sieve fraction as long as the Ar release is dominated by the 'small domains'; only when the 'small domains' are all outgassed and the largest 'domain' size starts contributing a significant proportion of the degassed Ar, there will be a difference in the diffusivity equal to the ratio $(r_{max}\ (fine)/r_{max}\ (coarse))^2$. Considering that the median grain radii $r$ of the present samples differ by a factor of about 2.5, the frequency factors $D/r_{max}^2$ should differ by a factor of 6.

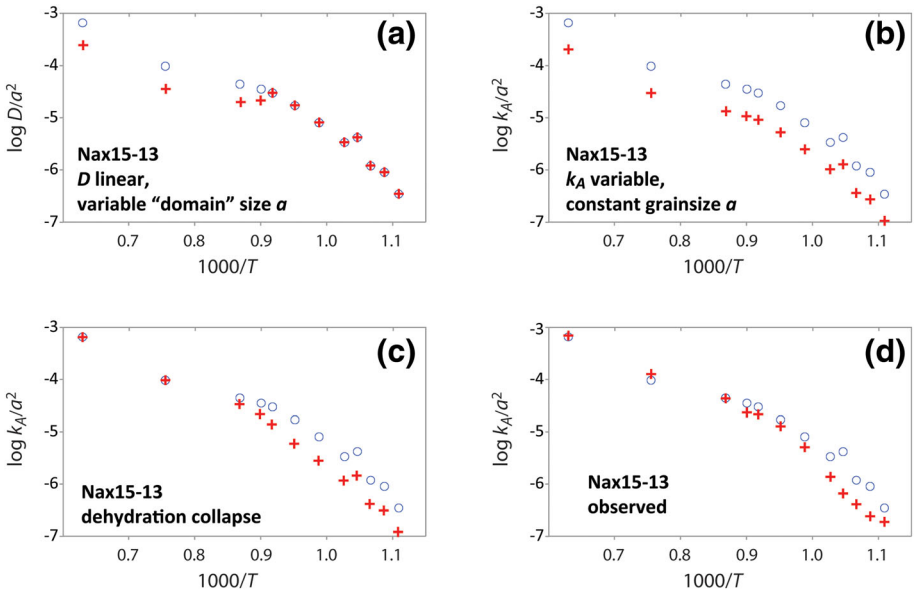


**FIGURE 5** Predicted Arrhenius trajectories for coarse and fine sieve fractions of the same monomineralic material, here exemplified for the argument's sake by mica NAX15-13 (even though it is clearly not monomineralic; see Figures 3 and 4). The Ar degassing rate $k_A$ is shown as a function of temperature (whereby the abscissa, $1000/T$, is given in $K^{-1}$). The trajectories are predicted by different models for the mechanism controlling the Ar degassing rate $k_A$. In model (a) the rate constant $k_A$ is assumed to be identical to $D/a^2$, whereby the diffusion constant $D$ is assumed as constant and all departures from Arrhenian linearity are attributed to variable "domain" sizes. The predicted trajectory of the coarse sieve fraction (crosses) overlaps with that of the fine sieve fraction (open circles) up to a certain temperature, then becomes lower by a factor equal to the square of the grain size ratio. In model (b), the degassing rate of white mica follows Fick's law with a fixed grain size. This applies to anhydrous phases such as K-feldspar; the Arrhenius trajectory is predicted and observed to consist of two parallel nonlinear trajectories (Chafe et al., 2014), whose vertical distance is the square of the grain size ratio. As the crystal structure, being anhydrous, remains approximately stable, the rate constant $k_A$ could be viewed as apparent diffusivity. (c) The degassing rate for the collapsing structure of a hydrous mineral is similar to Figure 5b up to the temperature at which the collapse sets in; during and after the collapse, Ar is released at the same rate from both fine and coarse sieve fractions, and the trajectories merge. (d) The observed degassing rate of NAX15-13 is incompatible with models (a) and (b) and compatible with (c).

Figure 5b draws on the observations pertaining to the K-feldspar archetype, MH-10 (Chafe et al., 2014). The measured degassing rate was observed to scale proportionally to the square of the grain radii from the lowermost furnace temperatures all the way to melting. This requires that the Arrhenian trajectory is kinked because it reflects additional effects that predominate over Fick's law, and that do not depend on grain size, and that proceed from the feldspar's by and large stable crystal structure. If the in vacuo degassing of WM behaved in the same way as that of anhydrous feldspar, the coarse fraction would have an apparent diffusivity lower than that of the fine fraction by a factor of 6, all the way from low to high furnace temperatures.

However, unlike feldspars, WM is well-known to dehydroxylate (Zimmermann, 1970) above a critical temperature (Heller-Kallai & Lapides, 2015 and references therein). During this process, the cell parameters change and the crystal structure collapses (Zimmermann, 1970). The dehydration reaction produces K-feldspar and corundum (Evans, 1965). As dehydroxylation starts at the grain surface, small crystals are expected to undergo faster collapse at lower temperature than large ones; this may explain the different temperatures reported in the literature for the onset of dehydroxylation, as experimenters (Heller-Kallai & Lapides, 2015, and references therein) used widely variable starting grain sizes. Sample-specific differences also account for large variations in the dehydration temperatures and rates (Zimmermann, 1970). In the present case, with surface/volume ratio variations limited to approximately 2.5, only small shifts in the peak of dehydroxylation are predicted (and indeed observed, see below). The predicted Arrhenius trajectories of the two sieve fractions are shown in Figure 5c. Initially, the fine fraction should degas faster by a factor of 6. Around 800°C (i.e. $1000/T \approx 0.9$) dehydroxylation causes the abovementioned structure collapse with accompanying formation of Kfs + Crn. When the collapse is concluded and the anhydrous structure of the Kfs + Crn reaction product is settled, the Arrhenius trajectory is controlled by the Ar release out of Kfs + Crn, which presumably forms a porous sinter (as the molar volume of WM is

larger than that of its reaction products), such that the degassing rate $k_A$ becomes independent of the grain size of the starting reagent.

The observed data for the coarse fraction (Figure 5d) support the prediction depicted in Figure 5c.

The degassing rates $k_A$ of the four WM separates are shown as a function of $T$ in Figure 6. They all show similar behaviour: At low temperature, the slope corresponds to an activation energy $E$ around 200 kJ/mol, whereby individual frequency factors are different; then around $x = 0.9$ (i.e. $T \approx 800°C$), the fine and the coarse fraction of every sample become coincident. Because the analysed separates were polymineralic (Figures 3 and 4), the bulk degassing rate is the sum of unrelated degassing rates of the various phases present. This sum is not expected to be linear and indeed is not (see also Chafe et al., 2014).

An alternative way to present the degassing rate is the differential release plot (Merrihue & Turner, 1966; Villa, 2021; Villa et al., 2000), in which the fraction of Ar released in each heating step is plotted as a function of temperature. In the general case, heating schedules may consist of differently spaced temperature steps of different duration. To account for these differences and to highlight the temperature intervals with the highest degassing rate, Villa et al. (2000) normalized the differential release of each step, $k_A$, to the temperature difference pertaining to that step, $\Delta T$, and the square root of the duration of the step, $\sqrt{t}$. The latter term is required if the degassing rate is assumed to proceed from Fickian diffusion; as in that case, the gas release is approximately proportional to $\sqrt{t}$. Since this assumption is very likely to be incorrect for hydrous minerals (Hetherington & Villa, 2007; Villa, 2021), the degassing rate may not depend on $\sqrt{t}$. The most robust approach to correctly estimating the degassing rate is using identical step durations, making the $\sqrt{t}$ term constant for all steps and effectively cancelling it out.

Observations on hydrous minerals (Villa, 2021) indicate that the peak of the differential release $k_A/(\Delta T \times \sqrt{t})$ coincides with the structural collapse due to dehydration. Thus, the observation by Wijbrans and McDougall (1986) that phengite and muscovite release Ar at different temperature (cfr. Figure 2 above) is best explained by the different binding energy of the OH groups. The exact collapse temperatures are not even expected to be identical for all phengites or for all muscovites, as individual samples of WM polymorphs are not strictly isochemical with the ideal end-members and therefore very likely to show subtle differences in their average interatomic bond length and strength. The stepheating protocol with its discrete temperature increases may apparently magnify such small differences by binning: the dehydration peaks of two samples may well be quite close in temperature, but due to the discontinuous nature of stepheating, the Ar released from each may end up in different discrete heating steps. The following discussion and graphics will therefore report the heating step number (furnace temperatures are given in the supporting information Table S1). What is most relevant is the approximately 150°C difference between the dehydration/degassing peaks of phengite and muscovite.

The differential release $k_A/(\Delta T \times \sqrt{t})$ of the mica separates is shown in Figure 7. A note of caution in the interpretation of the differential release diagrams is that an ideally monomineralic mica would yield a single peak, approximately bell-shaped, which describes the progressive structural collapse above the dehydration threshold temperature and the ensuing release of Ar (Villa, 2021). In a polymineralic (Figure 3) sample such as the Naxos micas, it is expected, and indeed observed, that different

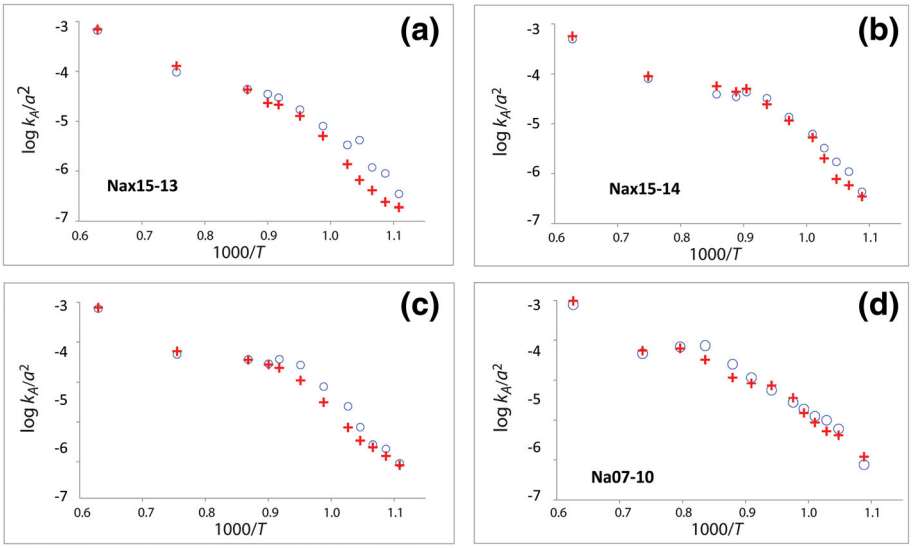


**FIGURE 6** Arrhenius diagrams of the four analysed white mica samples. (a) NAX15-13, (b) NAX 15-14, (c) NAX15-24, (d) Na07-10. The sieve sizes are shown as crosses (coarse) and open circles (fine). Because all studied samples are polymineralic, the bulk degassing rate $k_A$ is the sum of the unrelated degassing rates of each mineral present in the mixture. This bulk sum is not expected to be linear.

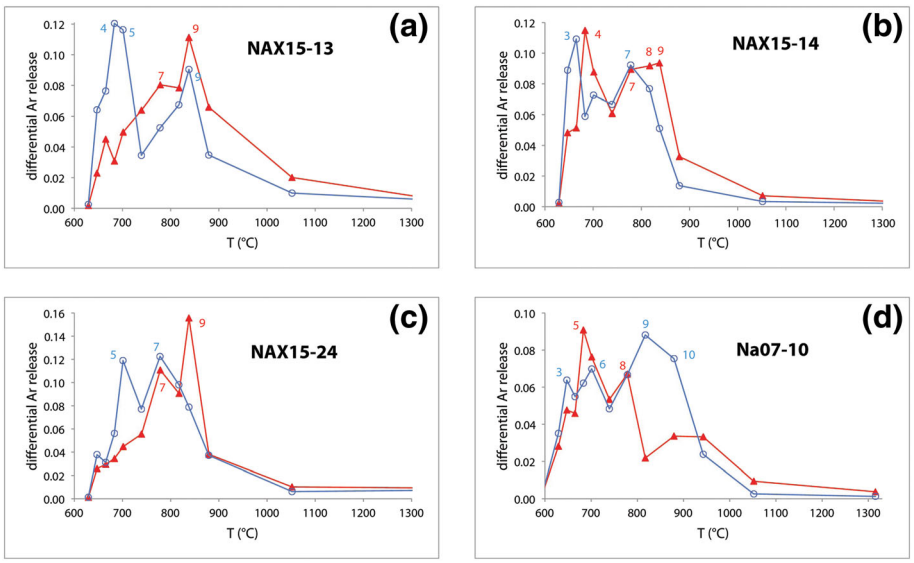


**FIGURE 7** Differential Ar release plots. Sieve size symbols as in Figure 4. (a, b) High-grade sample pair NAX15-13 and -14; (c, d) Lower-grade sample pair NAX15-24 and Na07-10; the latter show more spread-out degassing peaks.

bell-shaped release curves are superposed, each pertaining to the degassing of a separate mineral species. The two high-grade samples NAX15-13 and -14 show two, clearly resolved, major degassing peaks. In addition to the two major peaks, there may be two additional minor degassing peaks; this is not well resolved by the present experiment, but the main message is that there are *at least* two major mineral phases in the WM separate, whose discrimination is demonstrated here. In both samples, the coarse fraction and the fine fraction show one degassing peak corresponding to the 838°C step. This coincident release peak falls well in the temperature range of muscovite structural breakdown established by Zimmermann (1970) and is proposed here to identify the structural breakdown of one single generation of WM. This evidence will be supported by two additional arguments below.

In addition to the 838°C peak, the fine fractions of NAX15-13 and -14 as well as the coarse fraction of NAX15-14 show a degassing peak in the 680–700°C steps (Figure 7a,b). Since the peak around 680°C is not precisely overlapping for the four size fractions of NAX15-13 and -14, it is well plausible that a third (or even a fourth) WM generation is present in different amounts in the four separates. Note that our observation, visualized in Figure 3, is that four heterochemical WM generations are recognized. If the 838°C degassing peak is the structural breakdown of one WM generation, then it is most likely that the 700°C degassing peak corresponds to the structure breakdown of a both chemically and chronologically different mica generation. This is supported by the well-known observation that muscovite releases most of its Ar at lower temperature than phengite (Wijbrans & McDougall, 1986). The identification of the 838°C peak as HP phengite and of the 700°C peak as retrograde muscovite is also evident from the Cl/K signature and the age (see Section 4.4).

In the lower-grade sample NAX15-24 (Figure 7c), the 838°C peak in the coarse sieve fraction occurs at a slightly lower temperature, and degassing peaks are less sharp. The lower degassing temperature might be related to the lower metamorphic grade, under which a different mica polytype would have been formed with less tight interatomic bonds (Abbott & Burnham, 1988). The smearing of the degassing peaks is probably related to the presence of several distinct, albeit similar, mica varieties in what we have grouped as 'HP' and 'retrograde' micas. It must be pointed out that the temperature of the degassing peak is not sufficient on its own to identify the degassing phase with certainty; it is necessary to establish the context between the degassing behaviour and the common denominator correlations such as Ar/K versus Cl/K and Ar/K versus Ca/K (see Section 4.4). Sample Na07-10 was degassed with a temperature sequence different from the others; the fine fraction has its highest degassing rate between 817°C and 879°C, whereas that degassing peak is prominently absent from the coarse fraction. Other degassing peaks between 647°C and 701°C are only roughly reproduced in the two size fractions.

## 4.4 | Chemical signatures and ages

The least debatable age on Naxos is that of the Miocene HT event. In our samples, it is recorded only partially, as no complete recrystallization was achieved, as was the case in most samples reported by Wijbrans and McDougall (1986).

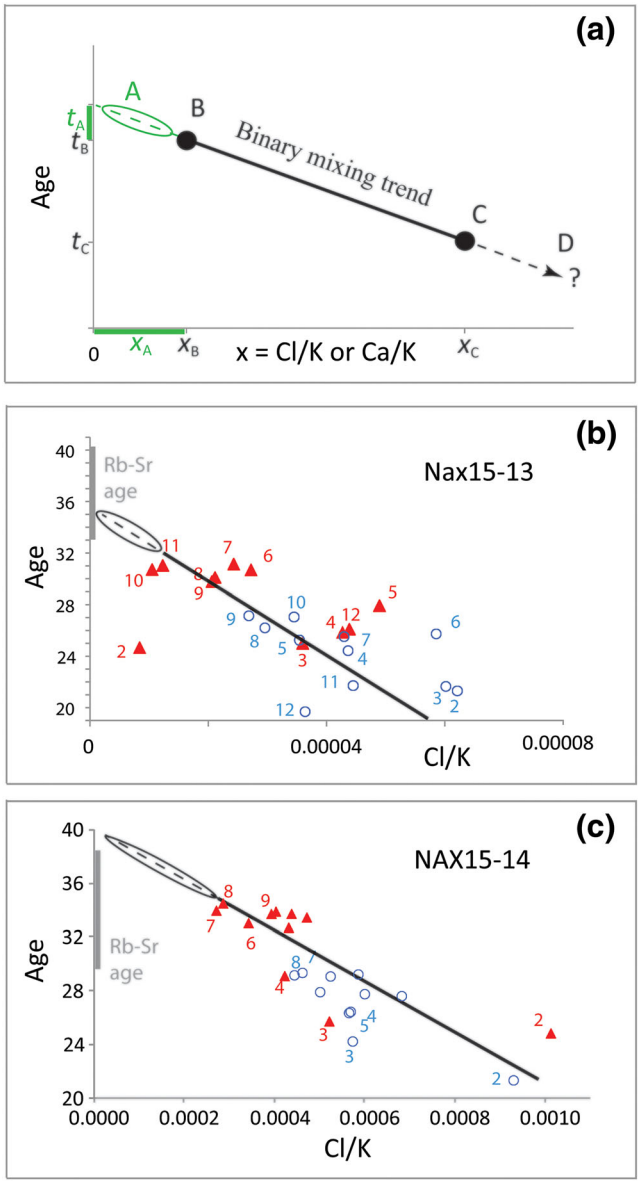


**FIGURE 8** Age versus composition common denominator three-isotope correlation diagrams. (a) The step age ($^{40}Ar^*/^{39}Ar_K$) is plotted against a chemical indicator, either Cl/K ($^{38}Ar_{Cl}/^{39}Ar_K$) or Ca/K ($^{37}Ar_{Ca}/^{39}Ar_K$). The straight line is a schematic illustration of a sample, in which all heating steps lie on the segment BC. In this diagram, points B and C (filled circles) represent the measured coordinates of the steps having the most extreme abscissa and ordinate values. The linear alignment indicates a binary mixing, whose end-members are not uniquely constrained by the heating steps: The true mixing end-members A and D may or may not be represented by the most extreme steps, B and C. In order to find A, the trend line must be extrapolated towards the upper left, whereas D lies on the extrapolation towards the lower right. In case the $x$ value of the end-members is independently known (e.g. by EPMA: Villa et al., 1996, their Figure 3), then the positions of points A and D are known. In the case of white micas, both Cl and Ca are near or below the detection limit of electron microprobes, and the only useful constraint on A is that $0 < x_A \leq x_B$; therefore $t_A \geq t_B$. Since $x_A > 0$, the position of end-member A must lie somewhere along the dashed line (marked by an open ellipse) and its coordinate values somewhere in the intervals marked by a thick segment on the $x$- and $y$-axes. End-member D is similarly underconstrained; the only relevant information is $0 \leq t_D \leq t_C$ and $x_D \geq x_C$. (b) Cl–age common denominator three-isotope correlation diagram for NAX15-13. Sieve size symbols as in Figure 4. A clear anticorrelation trend between age and Cl/K ratio is recognized; the dispersion of the points around ideal linearity indicates that other phases are also contributing Ar, corresponding to minor degassing peaks in Figure 7. The solid line represents the mixing between an old, Cl-poor phase (point B in Figure 8a) and a Cl-rich, young retrograde phase. It cannot be calculated by least squares fitting, as the data points do not belong to a single unimodal distribution; it is semiquantitatively estimated so as to pass through step 9 of the coarse fraction and step 5 of the fine fraction, that is, the peaks of the degassing rate of Cl-poor phengite and Cl-rich muscovite, respectively, as determined in Figure 7. The Rb-Sr isochron age (Table S2) is shown by a grey bar near the ordinate axis. The dashed line and ellipse mark the plausible range for end-member Cl-poor phengite. (c) Same diagram for NAX15-14. The Rb-Sr isochron age is shown for comparison.

The difficulties arise when one attempts to unravel the age of the Eocene HP event and to assign a meaning to the observed apparent ages. The context of the $^{39}Ar$-$^{40}Ar$ systematics provides additional help. After having identified the presence of two finely intergrown mica generations in NAX15-14 by the major element compositions (Figure 3), this bimodality is sought for and indeed found in the trace element Ca/K and Cl/K signature (Figure 4) and in the separate Ar degassing peaks (Figure 7). A combination of these three apparently unrelated observations on one and the same mineral separate is shown by a CDTIC diagram (Figure 8), in which the $^{40}Ar^*/^{39}Ar_K$, ratio of the two high-grade samples NAX15-13 and -14, is plotted against the $^{38}Ar_{Cl}/^{39}Ar_K$ ratio (both from Table S1). Both samples display a well-defined (albeit noisy) negative correlation between age and composition. Both size fractions of each sample should be interpreted on the basis of Figures 3 and 4. The coarse fraction of both samples is richer in a Cl-poor, old mica, which is intergrown (Figure 3) with a Cl-rich, younger mica. Incidentally, the Cl contents of the two WM polymorphs provide a semiquantitative constraint on the phengite–muscovite mass balance. Both predominant minerals in both samples are identified as WM basing on their nearly stoichiometric K concentrations (Table S1). The Cl concentrations, as discussed in

Section 4.2 basing on the fluid inclusion work by Siebenaller et al. (2013), discriminate between a Cl-poor phengite and a Cl-rich retrograde muscovite that was infiltrated and recrystallized by a Cl-rich fluid associated with the Miocene HT overprint and magmatism. Combining the CTDIC in Figure 8 with the differential release diagram (Figure 7) confirms that the chemical signatures of the steps associated with phengite (which is mainly degassed at higher temperature than muscovite: Wijbrans & McDougall, 1986), namely, steps 7, 8 and 9 (between 778°C and 838°C), are those with the lowest Cl/K ratios; the release peak of the retrograde muscovite, in steps 4 and 5 (683–701°C), is observed to have a substantially higher Cl/K ratio. This rounds off the argument that the two degassing peaks in Figure 7a,b pertain to not just mineralogically but also chronologically distinct mica generations, in accordance with the observations by Wijbrans and McDougall (1986), whereby the two diachronous mica generations also are compositionally different.

The necessary conclusions are that (i) the crushing and sieving has disproportionated the HP phengite and the HT muscovite among the coarse and fine fractions and (ii) each sieve fraction contains both mica generations: the coarse fraction is more enriched in phengite but contains μm-sized intergrowths of muscovite (Figure 3); the fine fraction also mostly consists of phengite, but the phengite/muscovite ratio is lower than in the coarse fraction. The fact that both trends in Figures 8 do not follow a single line but show considerable scatter is evidence that the simplified expressions 'HP phengite' and 'HT muscovite' ought to be rephrased as 'family of phengitic WMs produced over a finite time-span at generally high, but variable, pressure' and 'family of more muscovitic WMs produced in different moments during the continuous, protracted exhumation and increasingly high $T/P$ ratios'. For the sake of simplicity, we will keep the shorthand expressions, but it is vital to keep in mind that each of these two mica populations is not monogenetic and that minor phases also contribute a detectable amount of Ar.

The lower-grade sample pair NAX15-24 and Na07-10 shows several degassing peaks spreading over a broader temperature interval (Figure 7c,d). This indicates that these two samples are not predominantly binary mixtures but contain a significant proportion of a third (or even fourth) phase, as independently constrained by petrology (Figure 3) and by the CDTIC (see above). The preservation of a larger proportion of relicts requires a lesser degree of recrystallization of the protolith by the HP event. Due to this petrologic complexity, their CDTIC plots reflect ternary (or higher order) mixing, resulting in a point cloud enclosed by a polygon (following the systematics discussed by Villa, 2001). The complex pattern of NAX15-24 neither adds new insight nor discounts obtained from the high-grade pair. Sample Na07-10 from Kalados is discussed below.

Figure 8a–c provides semiquantitative constraints on the age of the 'HP phengite' by the extrapolation of the age-vs-Cl/K trend to the Cl/K value of the phengite end-member. Unfortunately, this Cl/K ratio is not well-known and cannot be measured with present electron microprobes with sufficient precision and sufficient spatial resolution. The difficulty is the very low Cl concentration in the phengitic end-members of NAX15-13 ($Cl/K \leq 2 \times 10^{-5}$, i.e. $[Cl] \leq 2$ ppm) and NAX15-14 ($[Cl] \leq 7$ ppm) and the very small beam diameter that any measurement should have in order to resolve phengite from the finely intergrown muscovite (Figure 3). We can only set upper and lower boundaries. If the structural collapse of pure phengite, with zero muscovite admixture, were exactly 838°C, then the age of the phengite would be exactly the 838°C step age, $29.77 \pm 0.03$ Ma (NAX15-13) and $34.05 \pm 0.03$ Ma (NAX15-14). However, it is more probable that all steps contain Ar released by both WM generations; in this case, the two values just mentioned are a strict lower limit, and the age information would be carried by the extrapolation. The most extreme possible extrapolation would be at $Cl/K = 0$ (a rather unlikely low value); the two extrapolated values are 39 and 35.7 Ma, respectively. In summary, a conservative confidence interval for the time, over which HP phengite grew, is 34–39 Ma, which corresponds to the retrograde path of the HP rocks from >16 to 9–10 kbar.

In the southern part of the island, a relict WM is observed. The presence of petrologic relicts is sufficient cause for isotopic inheritance (Villa, 1998). Suspiciously high ages are observed in Na07-10 (Table S1) and in sample N30A of Cao et al. (2018). The pre-Palaeocene ages (two high-temperature steps of Na07-10, plus the total gas age of N30A) are interpreted as a partly reset age of a pre-HP protolith. In a recent paper by Porkoláb et al. (2019) from a different locality in the CBU, it is clearly established that single WM grains may have vastly different bulk K-Ar ages. Their samples provide robust, unambiguous evidence of heterogeneous isotopic inheritance in mica grains of the blueschists that carry individually variable amounts of inherited pre-HP protolith relicts. In HP rocks, fluid circulation is heterogeneous and fluid-assisted recrystallization evidently took place in one part of their outcrop but not in others. This would lead to inheritance-free ages in parts of the outcrop, while only centimetres away the ages would be affected by inherited Ar. Our sample Na07-10 has a hump-shaped age spectrum (Figure 9) congruent with a mixture of the two WM generations revealed by EPMA. Following Wijbrans and McDougall's (1986) interpretation, one WM generation

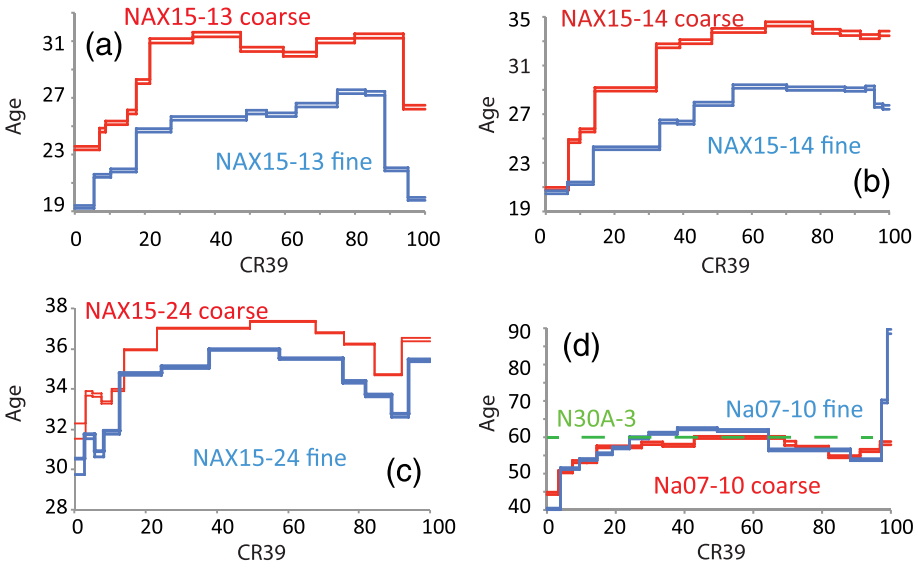


**FIGURE 9** Age spectra. CR39 is the cumulative $^{39}$Ar release. Other than reproducing the hump shape obtained in the literature, these eight age spectra provide an interesting but extremely limited insight on age systematics of polygenetic mineral mixtures. Note that in the sample that underwent two metamorphic overprints, Na07-10, the fine sieve fraction has an older apparent age than the coarse fraction. Sample N30A-3 from Cao et al. (2018) is shown as dashed line superposed on our sample Na07-10, as both were sampled in the same locality, Kalados.

has $t < 45$ Ma (the youngest step age), preceded by an old relict generation, in such mass balance as to yield a total gas age of 57 Ma. Supporting information Figure S1 shows a positive correlation between Cl/K and age for sample Na07-10. The Cl/K measurements have a high uncertainty, as does the regression line. However, the lower intercept of the regression (supposedly the low Cl HP mica) yields 44 ± 10 Ma (Mean Square of Weighted Deviates [MSWD] = 0.12); the upper limit of the trend is not well constrained, as the Cl/K ratio of the protolith mica is unknown, but the upper age limit has to be older or equal to the highest step age that defines the trend, 69 Ma. Note carefully that neither the 57 Ma total gas age nor the 69 Ma step age have geological significance, as they derive from the sum of two unrelated mica generations produced in two separate geological events. We also point out that the total gas age of Na07-10 is by no means exceptional, as Cao et al. (2018) reported an even older total gas age for their sample N30A. This implies, since the Kalados Bay outcrop preserves at least one pre-HP relict mica generation (Cao et al., 2018, their Figure 6), that their sample N30A should yield a hump-shaped age spectrum if re-analysed in sufficient detail and that the cusp of the hump should indicate inheritance of a (pre?-) Cretaceous protolith, as described in Tinos and Andros by Bulle et al. (2010) and Höhn et al. (2022), in the Eastern Cyclades by Koutsovitis et al. (2022), and especially in Naxos' neighbour island Donousa (Altherr et al., 1994).

## 4.5 | Summary of Ar observations

The simple interpretive model, whose quantification dates back to Purdy and Jäger (1976), namely, that all micas are monogenetic and that Ar is lost from muscovite exclusively by volume diffusion and that this diffusion is extremely fast (the 'closure temperature' being below 400°C!), is not able to explain any of the results on Naxos. What is observed instead is that all WMs in Naxos, and many others elsewhere, are polygenetic or even polymineralic mixtures, that Ar diffusion is slow ($D_0 < 0.01$ cm$^2$ s$^{-1}$, $E = 250$ kJ/mol; Villa et al., 2014) and that therefore the effect of faster processes like recrystallization and retrograde reactions in a chemically open system predominates over volume diffusion. The high Ar retentivity of muscovite is independently confirmed by Molecular Dynamics calculations (Nteme et al., 2022). Whenever micas are mixtures of heterochemical mica generations, it is possible to identify the chemical signatures and the age of the mixing end-members using the CDTIC option offered by $^{39}$Ar-$^{40}$Ar systematics (Villa & Hanchar, 2017).

The diffusivity coefficients derived empirically from WM samples in the Western Alps (Villa et al., 2014) translate to a WM 'closure temperature' for Ar loss of nearly 600°C, which agrees very well with that independently proposed by Hammerschmidt and Frank (1991), Di Vincenzo et al. (2004), Allaz et al. (2011), Laurent et al. (2017), Airaghi et al. (2018), Imayama et al. (2019) and

Nteme et al. (2022) and with the observed Ar inheritance in the Kalados samples (see below), which record a peak temperature of approximately 560°C (Peillod et al., 2017). The attempt to derive the diffusivity of mica by the first steps of in vacuo heating (Kula & Spell, 2012) should not be taken seriously, as the first heating steps have the unambiguous Ca/Cl/K signature of alteration clays, whose degassing rate bears no relation to that of WM.

The observation that Rb-Sr and K-Ar ages coincide (Figure 8b,c and supporting information Table S2) for the Naxos phengites, despite the much lower thermal diffusivity constant for Sr than for Ar (see below), is not compatible with temperature as the main factor controlling retention/loss of radiogenic Sr and Ar. This conclusion had already been demonstrated by Halama et al. (2018). The same inconsistency between observations and the model predictions of diffusion relates to the ages and chemical signatures (Rb/Sr and Cl/K element ratios) of different sieve fractions of the same sample. The main control on WM ages is instead the reaction, in a chemically open system, of Si-rich phengite to Al-Cl-rich muscovite.

Age spectra for the four analysed samples are shown in Figure 9. By now, it has been clearly established that age spectra offer an extremely restricted view of the information potentially provided by $^{39}$Ar-$^{40}$Ar systematics. Deconvolving a mixed age based only on the shape of the age spectrum is normally ambiguous and unsuccessful (Villa & Hanchar, 2017, their figure 7). The age spectra are shown here to highlight the identity of that limited part of our results with age spectra from the literature. All of our samples display the hump-shaped age spectra, known to be due to phengite–muscovite intergrowths since the artificial mixture reported by Wijbrans and McDougall (1986). $^{39}$Ar-$^{40}$Ar internal isochrons of non-cogenetic, non-equilibrated, non-isochronous minerals are not meaningful and are not considered. The age of the HT muscovite generation is constrained to be ≤20 Ma old by the lowest step ages in the present spectra, consistent with the age data (Wijbrans & McDougall, 1986) on the migmatites and the granitoid intrusions (Ring et al., 2018 and references therein). The observation, based on the spectra alone, that apparent $^{39}$Ar-$^{40}$Ar ages are older in the coarse grain size of three out of four samples could give the impression of higher diffusive Ar loss from the finer sieve sizes. However, Rb-Sr shows indistinguishable ages from the K-Ar chronometer all while not showing an age decrease with decreasing grainsize. This negates the main tenet of Purdy and Jäger's (1976) 'thermochronology', which asserted that bulk Rb-Sr ages of WM always had to be substantially older than the K-Ar ages of the same samples due to much higher 'closure temperatures'. What is even more important is that the bulk composition of the sieve fractions, as well as the Ca/Cl/K signatures of individual steps, demonstrates that the two size fractions analysed here have a different inventory of heterochemical, and diachronous, mica generations. The age of the coarse fraction is a mixed age between a Cl-poor, old phengite and a Cl-rich, young muscovite. The age of the fine fraction is a mixed age between the same two major endmembers — but, and here lies the rub, the mass proportions of phengite and muscovite are different, and the age of the mixture varies according to their mass balance. It cannot be seriously proposed to regard the fine size fraction as the diffusively rejuvenated aliquot of the same mineral making up the coarse fraction.

A pre-Eocene relict mica was observed in Kalados, at the southern tip of Naxos, both by us (Figure 8d) and by Cao et al. (2018). This is likely a relict of the regional amphibolite–greenschist facies basement, whose mica ages are Cretaceous elsewhere in the Cyclades islands (Laurent et al., 2017).

## 4.6 | Ar-Sr multichronometry

The Rb-Sr isochrons presented by Peillod et al. (2017), and summarized here in the supporting information Table S2, are apparently of limited reliability owing to their high overdispersion. However, the Rb-Sr apparent ages of the phengites NAX15-13 and -14 are indistinguishable from the $^{39}$Ar-$^{40}$Ar ages discussed above. We will first recall the petrologic framework, then illustrate how the chronometric systems illuminate the isotopic effects of petrology. The comparison of the K-Ar and Rb-Sr systems reveals the following:

(i) Since the separated WM fractions used in the present work and by Peillod et al. (2017) are mg-sized aliquots of the same hand-picked separate, it can be assumed that the phase inventory of the bulk formed by hundreds of grains is very similar. This phase inventory of all four samples is composed of at least two mica generations, recognized by microstructural analysis and by EPMA: a relict basement mica and HP phengite. In the two lower-grade samples NAX15-24 and Na07-10, the additional presence of paragonite is well visible. From the spread along the ordinate of the Cl/K-age CDTIC plot of samples NAX15-13 and -14 (Figure 8b, c), it is possible to infer a qualitative mass balance: the coarse-grained separates were mostly phengite. From the bulk ages of the two fractions (Table S1), one infers that the Miocene muscovite accounts for less than half of the fine fraction. This justifies the Rb-Sr isochron ages (Peillod et al., 2017) formed by two or three,

predominantly phengitic, WM fractions as a robust phengite age. The high MSWD of the Rb-Sr isochrons (Table S2) is a function of the variable admixture of non-cogenetic, non-isochronous phases in initial isotopic disequilibrium, such as the Miocene HT muscovite and/or paragonite and/or relict basement mica, whose effect is limited to creating overdispersion but not to shifting the mass balance of Rb and Sr and to grossly affect the isochron slope.

(ii) The Rb/Sr element ratio is variable between sieve fractions of the same sample (Peillod et al., 2017). This could, at least in principle, be due to a different budget of Rb-poor impurities in the sieve fractions. However, basing on the EPMA evidence that each sample is polymineralic and on the $^{39}Ar$-$^{40}Ar$ evidence that the phengite–muscovite modal proportions were disproportionated by crushing and sieving, we propose instead that the spread of the Rb/Sr element ratio is mainly a function of the Rb and Sr concentrations of the two principal coexisting WM generations.

(iii) An explanation designed to force a thermochronological interpretation on all mica ages would be that the lower $^{87}Sr/^{86}Sr$ ratios are due to selective diffusive loss of radiogenic $^{87}Sr^*$. This interpretation predicts apparent ages ('cooling ages') that are younger than the true formation age (Figure 10a). The diffusion trend is the downward black arrow, since $^{87}Sr^*$ loss lowers the $^{87}Sr/^{86}Sr$ ratio. The dashed and dotted lines illustrate the shallowing of the isochron slope, that is, the progressively younger ages of the finer grain sizes. The predictions of the thermochronological model do not match the observed data: in the two higher-grade samples NAX15-13 and -14, it is the coarse fraction which has the lower $^{87}Sr/^{86}Sr$ ratios (Peillod et al., 2017); this observation conflicts with the diffusionistic model that smaller grains lost more radiogenic $^{87}Sr$. Moreover, the observed Rb/Sr element ratios vary by a factor of 2. This might in principle be attributed to large amounts of impurities, despite prolonged hand-picking. In the present case, total $^{39}Ar$ concentrations on aliquots of the same separates allow the calculation of nearly stoichiometric K concentrations, reducing the importance of impurities. The most likely interpretation is that the formation of Miocene retrograde muscovite occurred in a chemically open system whereby advection/removal of soluble Rb and Sr by an aqueous fluid was the predominant mechanism.

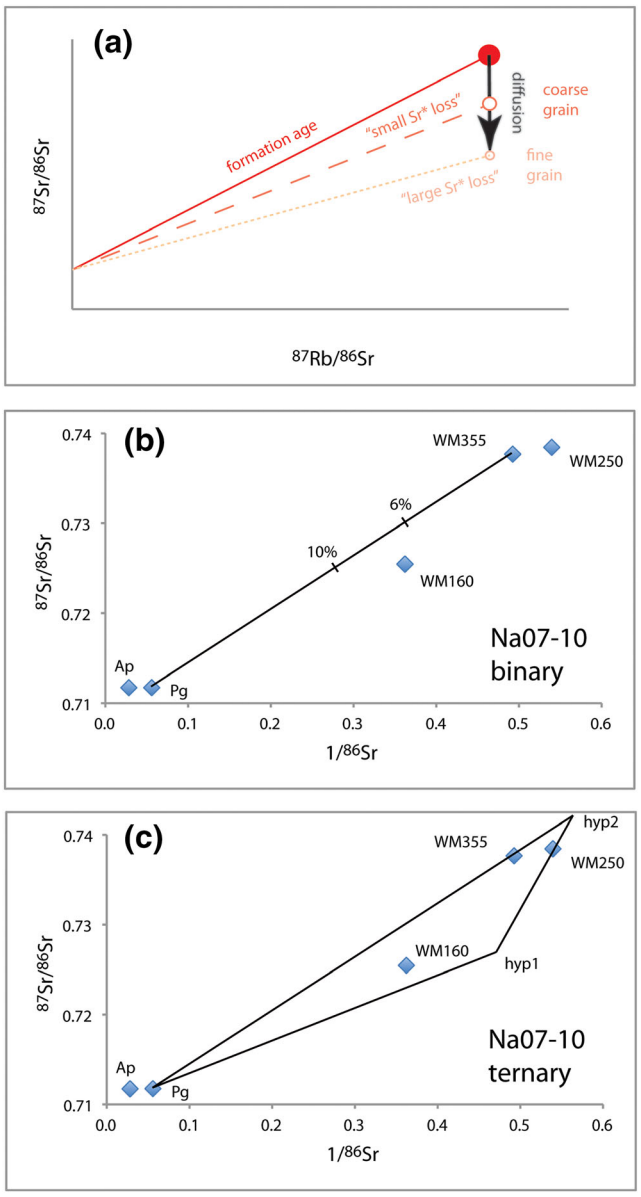


FIGURE 10 Legend on next page.

(iv) An observation-based discussion of the data needs to take into account their entirety, especially the fact that non-cogenetic, non-contemporaneous mineral phases were regressed together. The following discussion will best be focused on Na07-10 because of its documentedly polymineralic nature and of the necessity to explain the lack of age concordance between the Rb-Sr and K-Ar decay systems. Figure 10b shows the mixing diagram used for radiogenic isotopes: the abscissa is the reciprocal of the Sr concentration, and the ordinate is the $^{87}Sr/^{86}Sr$ ratio. Because the denominator is common, a binary mixing will be revealed only if the data define a straight

**FIGURE 10** Rb-Sr systematics. (a) Schematic illustration of the predicted effect of 'diffusional 87Sr* loss' on Rb-Sr isochron ages. Smaller grainsizes (dashed and dotted line) have younger apparent ages. (b) Common denominator mixing diagram for the Rb-Sr system. The two sieve fractions of sample Na07-10 analysed by $^{39}$Ar-$^{40}$Ar, WM355 and WM160, are shown together with Sr-rich apatite (Ap), paragonite (Pg) and the sieve fraction WM250 not available for $^{39}$Ar-$^{40}$Ar analysis. Binary mixing between WM355 and Pg would result in the solid line. Note that because of the much higher Sr concentration of Pg, a small admixture of Pg considerably shifts the point representing the WM355 + Pg mixture. The tick-mark labelled 10% represents a 1:9 mixing ratio between Pg and WM355. The Sr concentration measured in WM160 would be explained by a 6:94 mixing (tick-mark 6%) if the system was purely binary. The deviation of WM160 from the line requires a third phase in the mixture (see Figure 10c). (c) Same diagram as Figure 10b. In order to account for all four mica points, a minimum of three end-members are required: Pg and two hypothetical 'end-member' micas, hyp1 (provisionally proposed to be the relict cretaceous basement muscovite) and hyp2 (provisionally identified as the Eocene HP phengite). As the triangle sketched here is a minimum triangle, these end-members are strongly underconstrained: hyp2 could well plot further to the upper right, and hyp1 could plot anywhere below the WM250 and WM160 tie line in the horizontal rectangle defined by the vertices Pg and hyp2.

line. The data for Na07-10 define a broadly linear trend; however, individual points do not all lie on the mixing line between paragonite and the coarsest mica. We made the qualitative statement (see above) that the mineral prevailing by mass, that is, that contained in sieve fractions WM355 and WM250, controls the slope of the Rb-Sr isochron; the Sr concentration argument (Figure 10b) constrains semi-quantitatively the contribution of the Sr-rich paragonite to at most a few percent of the analysed separate. A precise quantitative assessment is made difficult by the presence of more than two end-members. Assuming that Na07-10 is composed of just three mica generations (Figure 10c; see below), the complexity of the system becomes immediately clear. An unfortunate complication is that since the hypothetical 'end-member micas' in Figure 10c (hyp1 and hyp2) are not constrained, we cannot estimate their Sr concentrations and thus cannot perform a mass balance calculation (a hint, motivated below, is that the influence on the Rb-Sr isochron age by hypothetical 'end-member mica' hyp1 was minor). Our argument in point (i) identifies HP phengite as the most abundant mica generation in the analysed aliquots and thus mostly controlling their Rb-Sr isochron ages. On the other hand, the $^{40}$Ar* budget requires that one old, inherited phase be more abundant in the WM160 fraction than in WM355. This phase corresponds to hyp1 in Figure 10c. Its age is not known, but it has to be older than the oldest steps measured by Cao et al. (2018) and in the present work, that is, Cretaceous (or older). The signature of the paragonite end-member would be recognized by a high $^{37}$Ar/$^{39}$Ar ratio, but because of the low modal abundance of paragonite in the analysed separate and the possible interference by minor plagioclase and calcite, it is not clear whether an Eocene age assignment (Figure S1) is accurate. The predictably low K concentration of paragonite, coupled to its low modal abundance, makes its contribution to the K-Ar system negligible. Thus, the apparent discrepancy of the K-Ar and Rb-Sr chronometers can be explained by a combined evaluation of EPMA analyses, mass balance and age inheritance: The inherited (pre-) Cretaceous basement mica, identified as hyp1 in Figure 10c, accounts for a large influence on the $^{40}$Ar* budget, but if its true (unconstrained) $^{87}$Sr/$^{86}$Sr ratios were sufficiently low (e.g. due to a low Rb/Sr element ratio or to a low initial $^{87}$Sr/$^{86}$Sr), then its influence on the Rb-Sr isochron slope would be minor. On the other hand, the Rb-Sr isochron slope is controlled by hyp2, whose influence on the $^{40}$Ar* budget is probably overrun by the inherited end-member hyp1.

(v) The coincidence of the Rb-Sr and K-Ar ages is unexplainable if only diffusion controlled the exchange of radiogenic daughter isotopes (e.g. Bosse et al., 2005). The laboratory determinations of Ar 'diffusivity' in hydrous minerals are notoriously unreliable (Villa, 2021); the only estimate on the relative diffusivities of Sr and Ar in silicates was provided by Cherniak and Watson (1992), who found that in anhydrous feldspar, the $Sr^{2+}$ ion diffuses $4 \times 10^4$ times less fast than the Ar atom, despite having the same activation energy (that required for the creation of Schottky defects: Villa, 2016). If there is such a large Ar-Sr difference in diffusivity for hydrous silicates as well, the coincidence of Sr retention and Ar retention in the Naxos samples conclusively rules out that thermal diffusion had a significant influence on them. The only way that Ar retention and Sr retention can be equal is by setting the radiometric clock only once, during the neocrystallization of phengite during the HP event, and never affecting it ever since. As the regional temperatures near the biotite-in isograd reached approximately 570°C for the

Miocene T-dominated overprint (Peillod, Majka, et al., 2021), the implication is that neither Ar nor Sr undergoes major loss from WM below 570°C. The $^{40}Ar^*$ inheritance in preserved Cretaceous relicts in Na07-10 (which underwent a HP temperature of approximately 560°C) confirms this finding.

(vi) The coincidence of the Rb-Sr and K-Ar ages also provides decisive constraints to a long-standing problem in the interpretation of K-Ar ages: Are unexpected high K-Ar ages due to excess Ar ($^{40}Ar_{xs}$) or to inherited Ar ($^{40}Ar_{inh}$)? The difference between the two is not just a semantic one but a fundamental geochemical one about the role of fluids. $^{40}Ar_{xs}$ requires addition of parentless $^{40}Ar$ from an outside circulating fluid into the analysed mineral. $^{40}Ar_{inh}$ requires incomplete loss of true radiogenic $^{40}Ar^*$ from a relict mineral during the geological event being dated and is removed by fluid-induced recrystallization. Since fluid ingress in metamorphic rocks can be heterogeneous at all scales, recrystallization could take place in one part of an outcrop (or of a cm-sized portion of a rock) but not in others, causing age heterogeneity at the m-to-μm scale. In the present case, invoking $^{40}Ar_{xs}$ as the cause for unexpected high K-Ar ages in HP rocks would require finely tuned additions of parentless Ar (and possibly also of parentless Sr) to precisely yield a consistent age pattern at the scale of the entire island. A preferred explanation, following Occam's Razor, is that phengite K-Ar ages match Rb-Sr ages because both are formation ages, devoid of inheritance because micas were thoroughly recrystallized. A corollary is that none of the Naxos micas records a cooling age, since diffusive losses of radiogenic $^{40}Ar^*$ were negligible in the newly formed HP paragenesis and, a fortiori, allowed the patchy preservation of $^{40}Ar_{inh}$ in the lower-grade Kalados Bay samples Na07-10 (this work) and N30A (Cao et al., 2018).

(vii) Multichronometry, such as Rb-Sr versus K-Ar, is an important element of our general strategy to achieve an overdetermined system. Just as overdetermined Rb-Sr isochrons are the basis for deciding whether all information converges to a robust age assignment, our approach requires as much redundancy as possible throughout the project. Redundant sampling, as had been secured by Peillod et al. (2017), consists in collecting several samples from one and the same subunit of the studied unit, in the expectation that samples from each subunit define internally consistent *P–T–t* paths. The redundant sampling by Peillod et al. (2017) also included separation of several sieve sizes for each studied hand specimen, whose internal comparison proved essential in our discussion. Note that Rb-Sr versus K-Ar multichronometry is necessary but not always sufficient for a conclusive chronological framework (e.g. Bröcker et al., 2013). Other necessary pieces of information require a detailed microtextural characterization: Work by optical microscopy should always be supplemented by EPMA (element maps and point analyses), even if that is sometimes viewed as superfluous duplication by old-school petrographers. Despite our extensive textural, microchemical and petrologic groundwork, some of our $^{39}Ar$-$^{40}Ar$ data would remain ambiguous if taken out of context with the information on grain sizes, Rb-Sr systematics and the all-important 'forgotten' isotopes $^{38}Ar_{Cl}$ and $^{37}Ar_{Ca}$. As an example,

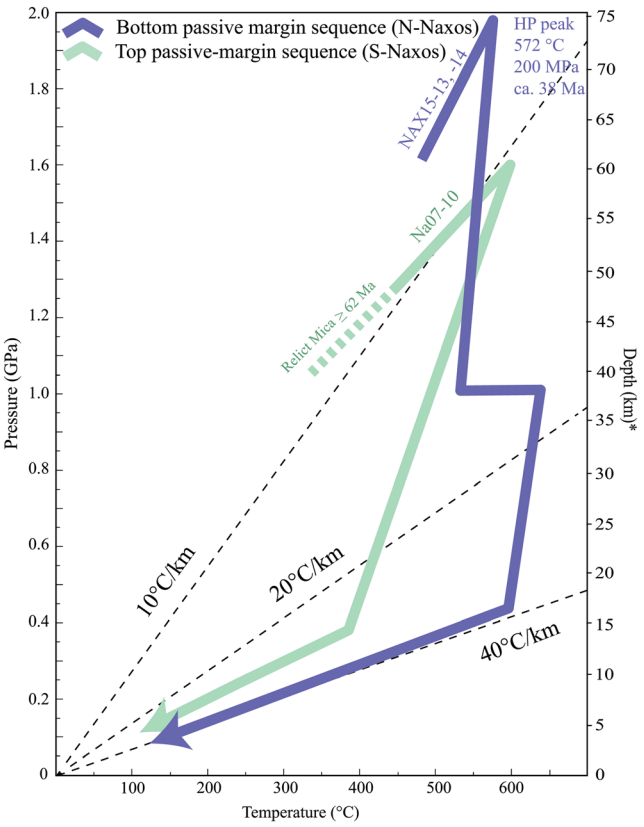


**FIGURE 11** Schematic *P–T–t* diagram, redrawn after Peillod, Majka, et al. (2021) and Peillod, Tehler, et al. (2021). *P–T–t* paths for the top of the middle-CBU nappe near Kalados Bay (in blue), the central section of the middle-CBU nappe (green path). Refer to yellow stars in Figure 1a for sample localities. Note the isobaric heating in the lower parts of the tectonic pile. Data were from Peillod et al. (2017), Peillod, Majka, et al. (2021), and Peillod, Tehler, et al. (2021).

the ground-breaking work by Wijbrans and coworkers in the 1980s (op. cit.), which was cutting-edge 36 years ago, lacked all of the vital pieces of information on microtextures, microchemistry, dependence of apparent ages on grain size and the full interpretive resources of the $^{39}$Ar-$^{40}$Ar and Rb-Sr dating methods. For that reason, Wijbrans and McDougall's (1988) age spectra, taken out of their necessary context, provided a questionable chronology for Naxos.

(viii) A final remark on the petrochronological–multichronometric approach illustrated here regards the legacy data from older literature. For those papers that decoupled mass spectrometric analyses from petrological groundwork, it is impossible to reconstruct which ones among the analysed samples contained relict micas with inherited Ar, which ones were subject to secondary retrogression, which ones record both and which ones record none. Some age estimates from the literature may be correct and some incorrect; however, it is not always explicitly clear which isotopic measurements had fulfilled the rather stringent prerequisites of petrochronology.

## 5 | CONCLUSIONS

The WM samples from Naxos offer both regional and general, petrochronological conclusions that are applicable to all samples containing polygenetic mica populations.

1. The petrological groundwork by Peillod et al. (2017, and references therein) enables us to propose the following *P*–*T*–*t* evolution (Figure 11). At least three WM generations recognized by EPMA are inextricably intergrown at the <<10 μm scale. The observation that major element concentrations undergo abrupt changes between heterochemical subgrains requires that diffusive re-equilibration of major elements was very subordinate and so was, by inference, that of trace elements (including Sr* and Ar*). These three different mica generations can be assigned to three events recorded by the Naxos samples: the formation of a greenschist–amphibolite facies basement in Cretaceous times; the HP metamorphism around 38 Ma, concordantly dated by Rb-Sr and K-Ar; and finally, retrograde reactions during exhumation, emphasized by the fluid aureole around the magmatic-migmatitic dome, which have produced a HT muscovite generation between ca. 11 and 20 Ma. The age of the prograde phase of the HP event is bracketed by the inheritance in WM samples from the southernmost (and lowest-grade) part of Naxos: Na07-10 analysed here and N30A (Cao et al., 2018) and by the subsequent Eocene peak of the HP event.

2. Regional metamorphic *P*–*T* conditions up to approximately 570°C were insufficient to achieve the complete diffusive reequilibration of both radiogenic daughters, $^{87}$Sr* and $^{40}$Ar*, since pre-peak ages are observed in heterochemical relicts, and internal isotopic disequilibrium is observed in all samples, both in their Sr and Ar isotope systematics. The retention of Sr* and Ar* is very high; therefore, fast diffusion rates sometimes proposed in the literature are not relevant in well-documented, real geological situations. Literature studies that did not take into account the role of isotopic inheritance could have obtained unrealistically high mineral ages; those studies that did not address retrograde reactions could have obtained unrealistically low mineral ages.

3. Multichronometric analyses provide strong constraints on the mechanisms controlling daughter isotope systematics and, by inference, on a reliable estimate of isotopic ages. The lack of a correlation between grain size and age also argues against a purely thermally induced loss of Sr* and Ar*. In the samples analysed here, both the Rb-Sr system and the K-Ar system record the HP formation ages. In the lowermost grade sample, the blueschist metamorphic conditions were insufficient to completely recrystallize the pre-HP minerals and Ar inheritance is manifested heterogeneously on a grain-by-grain scale. The Rb-Sr versus K-Ar comparison is essential to discriminate inherited Ar from excess Ar, the latter being absent from all samples analysed here.

4. The chemical signatures of WMs in different sieve sizes of the same sample are distinct. Crushing and sieving have disproportionated the two principal mica generations, HP phengite and HT muscovite.

5. The in vacuo release of Ar from WMs is neither consistent with the predictions of 'Discrete Domain' theory nor with Ar transport out of a stable crystal structure. The dehydration, structure collapse and

reaction of muscovite to K-feldspar plus corundum result instead in a pronounced peak in a differential release plot, in which muscovite and phengite display their well-known difference in collapse temperatures.

6. The differential Ar release peaks match the chemical (Ca/Cl/K) signature of the degassing phases. Additional detection by EPMA of minor alteration 'clays' accounts for irregular Ca/Cl/K systematics in the lowermost temperature part of the step heating experiments.

7. Disentangling the ages of the different WM generations uncompromisingly requires the combination of textural microanalysis, electron microprobe element mapping, multichronometric Rb-Sr versus K-Ar comparisons, differential Ar release plots and CDTIC diagrams. Whenever one of these essential pieces of information is missing, the chronological information becomes underconstrained and unreliable. It is highly recommended that all studies addressing metamorphic rocks apply this multidisciplinary petrochronological approach, as only the recognition of the context of the mass spectrometric data with all available petrogenetic constraints can provide reliable age constraints.

## ACKNOWLEDGEMENTS

Reviews by Valérie Bosse and Thomas Lamont and Editor Clare Warren greatly helped to clarify our presentation.

## ORCID

*Igor M. Villa* https://orcid.org/0000-0002-8070-8142
*Alasdair Skelton* https://orcid.org/0000-0002-3732-7993

## REFERENCES

Abbott, R. N. Jr., & Burnham, C. W. (1988). Polytypism in micas: A polyhedral approach to energy calculations. *American Mineralogist*, *73*, 105–118.

Airaghi, L., Warren, C. J., de Sigoyer, J., Lanari, P., & Magnin, V. (2018). Influence of dissolution/reprecipitation reactions on metamorphic greenschist to amphibolite facies mica $^{40}Ar/^{39}Ar$ ages in the Longmen Shan (eastern Tibet). *Journal of Metamorphic Geology*, *36*, 933–958. https://doi.org/10.1111/jmg.12420

Allaz, J., Berger, A., Engi, M., & Villa, I. M. (2011). The effects of retrograde reactions and of diffusion on $^{39}Ar$-$^{40}Ar$ ages of micas. *Journal of Petrology*, *52*, 691–716. https://doi.org/10.1093/petrology/egq100

Altherr, R., Kreuzer, H., Lenz, H., Wendt, I., Harre, W., & Dürr, S. (1994). Further evidence for a late cretaceous low-pressure/-high-temperature terrane in the Cyclades, Greece—Petrology and geochronology of crystalline rocks from the islands of Donoussa and Ikaria. *Chemie der Erde*, *54*, 319–328.

Avigad, D. (1998). High-pressure metamorphism and cooling on SE Naxos (Cyclades, Greece). *European Journal of Mineralogy*, *10*, 1309–1319. https://doi.org/10.1127/ejm/10/6/1309

Bolhar, R., Ring, U., & Allen, C. M. (2010). An integrated zircon geochronological and geochemical investigation into the Miocene plutonic evolution of the Cyclades, Aegean Sea, Greece: Part 1—Geochronology. *Contributions to Mineralogy and Petrology*, *160*, 719–742. https://doi.org/10.1007/s00410-010-0504-4

Bolhar, R., Ring, U., & Ireland, T. R. (2017). Zircon in amphibolites from Naxos, Aegean Sea, Greece: Origin, significance and tectonic setting. *Journal of Metamorphic Geology*, *35*, 413–434. https://doi.org/10.1111/jmg.12238

Bosse, V., Féraud, G., Ballèvre, M., Peucat, J. J., & Corsini, M. (2005). Rb–Sr and $^{40}Ar/^{39}Ar$ ages in blueschists from the Ile de Groix (Armorican Massif, France): Implications for closure mechanisms in isotopic systems. *Chemical Geology*, *220*, 21–45. https://doi.org/10.1016/j.chemgeo.2005.02.019

Bosse, V., & Villa, I. M. (2019). Petrochronology and hygrochronology of tectono-metamorphic events. *Gondwana Research*, *71*, 76–90.

Brichau, S., Ring, U., Ketcham, R. A., Carter, A., Stöckli, D., & Brunel, M. (2006). Constraining the long-term evolution of the slip rate for a major extensional fault system in the Central Aegean, Greece, using thermochronology. *Earth and Planetary Science Letters*, *241*, 293–306. https://doi.org/10.1016/j.epsl.2005.09.065

Bröcker, M., Baldwin, S., & Arkudas, R. (2013). The geological significance of $^{40}Ar/^{39}Ar$ and Rb–Sr white mica ages from Syros and Sifnos, Greece: A record of continuous (re)crystallization during exhumation? *Journal of Metamorphic Geology*, *31*, 629–646. https://doi.org/10.1111/jmg.12037

Bulle, F., Bröcker, M., Gärtner, C., & Keasling, A. (2010). Geochemistry and geochronology of HP mélanges from Tinos and Andros, cycladic blueschist belt, Greece. *Lithos*, *117*, 61–81. https://doi.org/10.1016/j.lithos.2010.02.004

Cao, S. Y., Neubauer, F., Bernroider, M., & Genser, J. (2018). Eocene high-pressure metamorphism and Oligocene retrogression on Naxos, Cyclades, Greece: Significance for Aegean tectonics and $^{40}Ar/^{39}Ar$ dating in polyphase metamorphic rocks. *Tectonophysics*, *745*, 66–94. https://doi.org/10.1016/j.tecto.2018.08.009

Çetinkaplan, M., Candan, O., Oberhänsli, R., Sudo, M., & Cenki-Tok, B. (2020). P–T–t evolution of the Cycladic Blueschist Unit in Western Anatolia/Turkey: Geodynamic implications for the Aegean region. *Journal of Metamorphic Geology*, *38*, 379–419. https://doi.org/10.1111/jmg.12526

Chafe, A. N., Villa, I. M., Hanchar, J. M., & Wirth, R. (2014). A re-examination of petrogenesis and $^{40}Ar/^{39}Ar$ systematics in the the chain of ponds K-feldspar: "diffusion domain" archetype versus polyphase hygrochronology. *Contributions to Mineralogy and Petrology*, *167*(5) paper 1010, 1–17.

Cherniak, D. J., & Watson, E. B. (1992). A study of strontium diffusion in K-feldspar, Na-K feldspar and anorthite using Rutherford backscattering spectroscopy. *Earth and Planetary Science Letters*, *113*, 411–425. https://doi.org/10.1016/0012-821X(92)90142-I

Di Vincenzo, G., Carosi, R., & Palmeri, R. (2004). The relationship between tectono-metamorphic evolution and argon isotope records in white mica: Constraints from in situ $^{40}$Ar-$^{39}$Ar laser analysis of the Variscan basement of Sardinia. *Journal of Petrology*, *45*, 1013–1043. https://doi.org/10.1093/petrology/egh002

Evans, B. W. (1965). Application of a reaction-rate method to the breakdown equilibria of muscovite and muscovite plus quartz. *American Journal of Science*, *263*, 647–667. https://doi.org/10.2475/ajs.263.8.647

Glodny, J., & Ring, U. (2022). The Cycladic Blueschist Unit of the Hellenic subduction orogen: Protracted high-pressure metamorphism, decompression and reimbrication of a diachronous nappe stack. *Earth-Science Reviews*, *224*, 103883. https://doi.org/10.1016/j.earscirev.2021.103883

Gorce, J. S., Caddick, M. J., Baxter, E. F., Dragovic, B., Schumacher, J. C., Bodnar, R. J., & Kendall, J. F. (2021). Insight into the early exhumation of the Cycladic Blueschist Unit, Syros, Greece: Combined application of zoned garnet geochronology, thermodynamic modeling, and quartz elastic barometry. *Geochemistry, Geophysics, Geosystems*, *22*, e2021GC009716. https://doi.org/10.1029/2021GC009716

Halama, R., Glodny, J., Konrad-Schmolke, M., & Sudo, M. (2018). Rb-Sr and in situ $^{40}$Ar/$^{39}$Ar dating of exhumation-related shearing and fluid-induced recrystallization in the Sesia zone (Western Alps, Italy). *Geosphere*, *14*, 1425–1450. https://doi.org/10.1130/GES01521.1

Hammerschmidt, K., & Frank, E. (1991). Relics of high pressure metamorphism in the Lepontine Alps (Switzerland) - $^{40}$Ar-$^{39}$Ar and microprobe analyses on white micas. *Schweizerische Mineralogische Und Petrographische Mitteilungen*, *71*, 261–274.

Heller-Kallai, L., & Lapides, I. (2015). Dehydroxylation of muscovite: Study of quenched samples. *Physics and Chemistry of Minerals*, *42*, 835–845. https://doi.org/10.1007/s00269-015-0767-4

Heri, A. R., Robyr, M., & Villa, I. M. (2014). Petrology and geochronology of the "muscovite standard" B4M. *Geological Society of London, Special Publication*, *378*, 69–78. https://doi.org/10.1144/SP378.2

Herviou, C., Verlaguet, A., Agard, P., Locatelli, M., Raimbourg, H., Lefeuvre, B., & Dubacq, B. (2021). Along-dip variations of subduction fluids: The 30–80 km depth traverse of the Schistes Lustrés complex (Queyras-Monviso, W. Alps). *Lithos*, *394-395*, 106168. https://doi.org/10.1016/j.lithos.2021.106168

Hetherington, C. J., & Villa, I. M. (2007). Barium silicates of the Berisal complex, Switzerland: A study in geochronology and rare-gas release systematics. *Geochimica et Cosmochimica Acta*, *71*, 3336–3347. https://doi.org/10.1016/j.gca.2007.05.001

Hetzel, R., & Reischmann, T. (1996). Intrusion age of Pan-African augen gneisses in the southern Menderes massif and the age of cooling after Alpine ductile extensional deformation. *Geological Magazine*, *133*, 565–572. https://doi.org/10.1017/S0016756800007846

Höhn, M., Bröcker, M., & Berndt, J. (2022). The Jurassic meta-ophiolitic rocks of Cape Steno, Andros, Greece: A high-pressure/low-temperature mélange with Pelagonian affinity in the Cycladic Blueschist Unit? *International Journal of Earth Sciences*, *111*, 949–968. https://doi.org/10.1007/s00531-022-02161-w

Imayama, T., Takeshita, T., Yi, K., & Fukuyama, M. (2019). Early Oligocene partial melting via biotite dehydration melting and prolonged low P/T metamorphism of the upper high Himalaya crystalline sequences in far-eastern Nepal. *Geological Society of London, Special Publication*, *481*, 147–173. https://doi.org/10.1144/SP481.2

Jansen, J. B. H., & Schuiling, R. D. (1976). Metamorphism on Naxos: Petrology and geothermal gradient. *American Journal of Science*, *276*, 1225–1253. https://doi.org/10.2475/ajs.276.10.1225

Jolivet, L., & Brun, J. P. (2010). Cenozoic geodynamic evolution of the Aegean. *International Journal of Earth Sciences*, *99*, 109–138. https://doi.org/10.1007/s00531-008-0366-4

Keay, S., Lister, G., & Buick, I. (2001). The timing of partial melting, Barrovian metamorphism and granite intrusion in the Naxos metamorphic core complex, Cyclades, Aegean Sea, Greece. *Tectonophysics*, *342*, 275–312. https://doi.org/10.1016/S0040-1951(01)00168-8

Koutsovitis, P., Soukis, K., Voudouris, P., Lozios, S., Ntaflos, T., Stouraiti, C., & Koukouzas, N. (2022). The late cretaceous magmatic arc of the South Aegean: Geodynamic implications from petrological and geochemical studies of granitoids from Anafi island (Cyclades – Greece). *International Geology Review*, *64*, 820–843. https://doi.org/10.1080/00206814.2021.1884906

Kuhlemann, J., Frisch, W., Dunkl, I., Kázmér, M., & Schmiedl, G. (2004). Miocene siliciclastic deposits of Naxos Island: Geodynamic and environmental implications for the evolution of the southern Aegean Sea (Greece). *Geological Society of America, Special Paper*, *378*, 51–65. https://doi.org/10.1130/0-8137-2378-7.51

Kula, J., & Spell, T. L. (2012). Recovery of muscovite age gradients by $^{40}$Ar/$^{39}$Ar vacuum furnace step-heating analysis. *Chemical Geology*, *304–305*, 166–174. https://doi.org/10.1016/j.chemgeo.2012.02.013

Kumerics, C., Ring, U., Brichau, S., Glodny, J., & Monié, P. (2005). The extensional Messaria shear zone and associated brittle detachment faults, Aegean Sea, Greece. *Journal of the Geological Society*, *162*, 701–721. https://doi.org/10.1144/0016-764904-041

Kylander-Clark, A. R. C., Hacker, B. R., & Cottle, J. M. (2013). Laser-ablation split-stream ICP petrochronology. *Chemical Geology*, *345*, 99–112. https://doi.org/10.1016/j.chemgeo.2013.02.019

Lamont, T. N., Searle, M. P., Waters, D. J., Roberts, N. M. W., Palin, R. M., Smye, A., Dyck, B., Gopon, P., Weller, O. M., & St-Onge, M. R. (2020). Compressional origin of the Naxos metamorphic core complex, Greece: Structure, petrography, and thermo- barometry. *GSA Bulletin*, *132*, 149–197. https://doi.org/10.1130/B31978.1

Laurent, V., Huet, B., Labrousse, L., Jolivet, L., Monié, P., & Augier, R. (2017). Extraneous argon in high-pressure metamorphic rocks: Distribution, origin and transport in the Cycladic Blueschist Unit (Greece). *Lithos*, *272-273*, 315–335. https://doi.org/10.1016/j.lithos.2016.12.013

Linnros, H., Hansman, R., & Ring, U. (2019). The 3D geometry of the Naxos detachment fault and the three-dimensional tectonic architecture of the Naxos metamorphic core complex,

Aegean Sea, Greece. *International Journal of Earth Sciences*, *108*, 287–300. https://doi.org/10.1007/s00531-018-1654-2

Maluski, H., Bonneau, M., & Kienast, J. R. (1987). Dating the metamorphic events in the Cycladic area: 39Ar/40Ar data from metamorphic rocks of the island of Syros (Greece). *Bulletin de la Société Géologique de France*, *8*, 833–842.

Martin, L., Duchêne, S., Deloule, E., & Vanderhaeghe, O. (2006). The isotopic composition of zircon and garnet: A record of the metamorphic history of Naxos, Greece. *Lithos*, *87*, 174–192. https://doi.org/10.1016/j.lithos.2005.06.016

Merrihue, C. M. (1965). Trace-element determinations and potassium-argon dating by mass spectroscopy of neutron-irradiated samples. *Transactions of the American Geophysical Union*, *46*, 125.

Merrihue, C. M., & Turner, G. (1966). Potassium-argon dating by activation with fast neutrons. *Journal of Geophysical Research*, *71*, 2852–2857. https://doi.org/10.1029/JZ071i011p02852

Müller, J., Koch-Müller, M., Rhede, D., Wilke, F. D., & Wirth, R. (2017). Melting relations in the system $CaCO_3$-$MgCO_3$ at 6 GPa. *American Mineralogist: Journal of Earth and Planetary Materials*, *102*, 2440–2449. https://doi.org/10.2138/am-2017-5831

Müller, W., Kelley, S. P., & Villa, I. M. (2002). Dating fault-generated pseudotachylytes: Comparison of $^{40}Ar/^{39}Ar$ stepwise-heating, laser-ablation and Rb/Sr microsampling analyses. *Contributions to Mineralogy and Petrology*, *144*, 57–77. https://doi.org/10.1007/s00410-002-0381-6

Nteme, J., Scaillet, S., Brault, P., & Tassan-Got, L. (2022). Atomistic simulations of $^{40}Ar$ diffusion in muscovite. *Geochimica et Cosmochimica Acta*, *331*, 123–142. https://doi.org/10.1016/j.gca.2022.05.004

Peillod, A., Majka, J., Ring, U., Drüppel, K., Patten, C., Karlsson, A., Włodek, A., & Tehler, E. (2021). Differences in decompression of a high-pressure unit: A case study from the Cycladic Blueschist Unit on Naxos Island, Greece. *Lithos*, *386–387*, 106043.

Peillod, A., Ring, U., Glodny, J., & Skelton, A. (2017). An Eocene/Oligocene blueschist-/greenschist facies P–T loop from the Cycladic Blueschist Unit on Naxos Island, Greece: Deformation-related re-equilibration vs. thermal relaxation. *Journal of Metamorphic Geology*, *35*, 805–830. https://doi.org/10.1111/jmg.12256

Peillod, A., Tehler, E., & Ring, U. (2021). Quo vadis Zeus: Is there a Zas shear zone on Naxos Island, Aegean Sea, Greece? A review of metamorphic history and new kinematic data. *Journal of the Geological Society*, *178*, jgs2020-217. https://doi.org/10.1144/jgs2020-217

Porkoláb, K., Willingshofer, E., Sokoutis, D., Creton, I., Kostopoulos, D., & Wijbrans, J. (2019). Cretaceous-Paleogene tectonics of the Pelagonian zone: Inferences from Skopelos island (Greece). *Tectonics*, *38*, 1946–1973. https://doi.org/10.1029/2018TC005331

Purdy, J. W., & Jäger, E. (1976). K-Ar ages on rock-forming minerals from the Central Alps. *Memorie dell'Istituto di Geologia e Mineralogia dell'Università di Padova*, *30*, 3–31.

Reynolds, J. H. (1963). Xenology. *Journal of Geophysical Research*, *68*, 2939–2956. https://doi.org/10.1029/JZ068i010p02939

Ring, U., Glodny, J., Peillod, A., & Skelton, A. (2018). The timing of high-temperature conditions and ductile shearing in the footwall of the Naxos extensional fault system, Aegean Sea, Greece. *Tectonophysics*, *745*, 366–381. https://doi.org/10.1016/j.tecto.2018.09.001

Ring, U., Glodny, J., Will, T., & Thomson, S., (2007). An Oligocene extrusion wedge of blueschist-facies nappes on Evia, Aegean Sea, Greece: Implications for the early exhumation of high-pressure rocks. *Journal of the Geological Society*, *164*, 637–652.

Ring, U., Glodny, J., Will, T., & Thomson, S. (2010). The Hellenic subduction system: High-pressure metamorphism, exhumation, normal faulting, and large-scale extension. *Annual Review of Earth and Planetary Sciences*, *38*, 45–76. https://doi.org/10.1146/annurev.earth.050708.170910

Ring, U., & Layer, P. W. (2003). High pressure metamorphism in the Aegean, eastern Mediterranean: Underplating and exhumation from the Late Cretaceous until the Miocene to recent above the retreating Hellenic subduction zone. *Tectonics*, *22* (3), 1022.

Ring, U., Will, T., Glodny, J., Kumerics, C., Gessner, K., Thomson, S., Güngör, T., Monié, P., Okrusch, M., & Drüppel, K. (2007). Early exhumation of high-pressure rocks in extrusion wedges: Cycladic blueschist unit in the eastern Aegean, Greece, and Turkey. *Tectonics*, *26*, TC2001. https://doi.org/10.1029/2005TC001872

Rivera, T. A., Storey, M., Zeeden, C., Hilgen, F. J., & Kuiper, K. (2011). A refined astronomically calibrated $^{40}Ar/^{39}Ar$ age for Fish Canyon sanidine. *Earth and Planetary Science Letters*, *311*, 420–426. https://doi.org/10.1016/j.epsl.2011.09.017

Seward, D., Vanderhaeghe, O., Siebenaller, L., Thomson, S., Hibsch, C., Zingg, A., Holzner, P., Ring, U., & Duchêne, S. (2009). Cenozoic tectonic evolution of Naxos Island through a multi-faceted approach of fission-track analysis. *Geological Society of London, Special Publication*, *321*, 179–196. https://doi.org/10.1144/SP321.9

Siebenaller, L., Boiron, M.-C., Vanderhaeghe, O., Hibsch, C., Jessell, M. W., Andre-Meyer, A.-S., France-Lanord, C., & Photiades, A. (2013). Fluid record of rock exhumation across the brittle–ductile transition during formation of a metamorphic core complex (Naxos Island, Cyclades, Greece). *Journal of Metamorphic Geology*, *31*, 313–338. https://doi.org/10.1111/jmg.12023

Skelton, A., Peillod, A., Glodny, J., Klonowska, I., Månbro, C., Lodin, K., & Ring, U. (2019). Preservation of high-P rocks coupled to rock composition and the absence of metamorphic fluids. *Journal of Metamorphic Geology*, *37*, 359–381. https://doi.org/10.1111/jmg.12466

Tomaschek, F., Kennedy, A., Villa, I. M., Lagos, M., & Ballhaus, C. (2003). Zircons from Syros, Cyclades, Greece—Recrystallization and mobilization of zircon during high-pressure metamorphism. *Journal of Petrology*, *44*, 1977–2002. https://doi.org/10.1093/petrology/egg067

Tual, L., Smit, M. A., Cutts, J., Kooijman, E., Kielman-Schmitt, M., Majka, J., & Foulds, I. (2022). Rapid, paced metamorphism of blueschists (Syros, Greece) from laser-based zoned Lu-Hf garnet chronology and LA-ICPMS trace element mapping. *Chemical Geology*, *607*, 121003. https://doi.org/10.1016/j.chemgeo.2022.121003

Turner, G. (1988). Hydrothermal fluids and argon isotopes in quartz veins and cherts. *Geochimica et Cosmochimica Acta*, *52*, 1443–1448. https://doi.org/10.1016/0016-7037(88)90214-1

Uunk, B., Brouwer, F., de Paz-Álvarez, M., van Zuilen, K., Huybens, R., van't Veer, R., & Wijbrans, J. (2022). Consistent detachment of supracrustal rocks from a fixed subduction depth in the Cyclades. *Earth and Planetary Science Letters*, *584*, 117479. https://doi.org/10.1016/j.epsl.2022.117479

Vanderhaeghe, O. (2004). Structural development of the Naxos migmatite dome. *Geological Society of America Special Papers*, *380*, 211–227. https://doi.org/10.1130/0-8137-2380-9.211

Vanderhaeghe, O., Kruckenberg, S. C., Gerbault, M., Martin, L., Duchêne, S., & Deloule, E. (2018). Crustal-scale convection and diapiric upwelling of a partially molten orogenic root (Naxos dome, Greece). *Tectonophysics*, *746*, 459–469. https://doi.org/10.1016/j.tecto.2018.03.007

Villa, I. M. (1998). Isotopic closure. *Terra Nova*, *10*, 42–47. https://doi.org/10.1046/j.1365-3121.1998.00156.x

Villa, I. M. (2001). Radiogenic isotopes in fluid inclusions. *Lithos*, *55*, 115–124. https://doi.org/10.1016/S0024-4937(00)00041-4

Villa, I. M. (2016). Diffusion in mineral geochronometers: Present and absent. *Chemical Geology*, *420*, 1–10. https://doi.org/10.1016/j.chemgeo.2015.11.001

Villa, I. M. (2021). The in vacuo release of Ar from minerals: 1. Hydrous minerals. *Chemical Geology*, *564*, 120076. https://doi.org/10.1016/j.chemgeo.2021.120076

Villa, I. M. (2022). Dating deformation: The role of atomic-scale processes. *Journal of the Geological Society*, *179*(5), jgs2021-098. https://doi.org/10.1144/jgs2021-098

Villa, I. M., Bucher, S., Bousquet, R., Kleinhanns, I. C., & Schmid, S. M. (2014). Dating polygenetic metamorphic assemblages along a transect through the Western Alps. *Journal of Petrology*, *55*, 803–830. https://doi.org/10.1093/petrology/egu007

Villa, I. M., Grobéty, B., Kelley, S. P., Trigila, R., & Wieler, R. (1996). Assessing Ar transport paths and mechanisms for McClure Mountains hornblende. *Contributions to Mineralogy and Petrology*, *126*, 67–80. https://doi.org/10.1007/s004100050236

Villa, I. M., & Hanchar, J. M. (2017). Age discordance and mineralogy. *American Mineralogist*, *102*, 2422–2439. https://doi.org/10.2138/am-2017-6084

Villa, I. M., Hermann, J., Müntener, O., & Trommsdorff, V. (2000). $^{39}$Ar -$^{40}$Ar dating of multiply zoned amphibole generations (Malenco, Italian Alps). *Contributions to Mineralogy and Petrology*, *140*, 363–381. https://doi.org/10.1007/s004100000197

Wijbrans, J. R., & McDougall, I. (1986). $^{40}$Ar/$^{39}$Ar dating of white micas from an Alpine high-pressure metamorphic belt on Naxos (Greece): The resetting of the argon isotopic system. *Contributions to Mineralogy and Petrology*, *93*, 187–194. https://doi.org/10.1007/BF00371320

Wijbrans, J. R., & McDougall, I. (1988). Metamorphic evolution of the Attic Cycladic Metamorphic Belt on Naxos (Cyclades, Greece) utilizing $^{40}$Ar/$^{39}$Ar age spectrum measurements. *Journal of Metamorphic Geology*, *6*, 571–594. https://doi.org/10.1111/j.1525-1314.1988.tb00441.x

Wijbrans, J. R., Schliestedt, M., & York, D. (1990). Single grain argon laser probe dating of phengites from the blueschist to greenschist transition on Sifnos (Cyclades, Greece). *Contributions to Mineralogy and Petrology*, *104*, 582–593. https://doi.org/10.1007/BF00306666

Zimmermann, J. L. (1970). Contribution à l'étude de la déshydratation et de la libération de l'argon des micas. *Geochimica et Cosmochimica Acta*, *34*, 1327–1350. https://doi.org/10.1016/0016-7037(70)90045-1

## SUPPORTING INFORMATION

Additional supporting information can be found online in the Supporting Information section at the end of this article.

**Figure S1.** Cl/K–age correlation diagram for sample Na07–10.

**Table S1.** Complete Ar stepheating data.

**Table S2.** Summary of Rb-Sr data by Peillod et al. (2017) on the four samples analysed here. Uncertainties are given at the 95% confidence level; wm (3) refers to 3 sieve size fractions of white mica.

**How to cite this article:** Villa, I. M., Glodny, J., Peillod, A., Skelton, A., & Ring, U. (2023). Petrochronology of polygenetic white micas (Naxos, Greece). *Journal of Metamorphic Geology*, *41*(3), 401–423. https://doi.org/10.1111/jmg.12700